

# Fluxgate Current Sensor for Superconducting Applications in Aerospace

Author: Callum Mooney

Student Number: \*

Supervisors: \*

Word Count: 8991

I hereby declare that this work has not been submitted for any other degree/course at this University or any other institution and that, except where reference is made to the work of other authors, the material presented is original and entirely the result of my own work at the University of Strathclyde under the supervision of \*.

4th April 2025

## **Abstract**

This project presents the theory, design, simulation, and implementation of a fluxgate current sensor. Commissioned by Supply Design Limited, the sensor was initially developed to operate under cryogenic conditions for future superconducting applications within the aerospace sector. This report documents the complete design process, beginning with an investigation into the fluxgate operating principle, followed by an evaluation of various topologies and key design decisions. High-level software implementation was conducted using LTspice and MATLAB/Simulink, and later expanded into low-level models incorporating realised peripherals and multi-core configurations. Non-ideal testing of the two-core closed-loop topology demonstrated an accuracy of 97.6%. The hardware development process is also presented, including a custom PCB design integrating the required signal processing elements for current measurement. Although time constraints prevented full hardware implementation, the software results and limited experimental testing verify the fluxgate operating principle and confirm its viability as a non-contact current measurement solution.

# Contents

<b>List of Figures</b>	<b>vi</b>
<b>List of Tables</b>	<b>vii</b>
<b>Nomenclature</b>	<b>vii</b>
<b>1 Introduction &amp; Motivation</b>	<b>1</b>
<b>2 Literature Review</b>	<b>5</b>
2.1 Fluxgate Operating Principle . . . . .	5
2.1.1 Hysteresis in Ferromagnetic Cores . . . . .	5
2.1.2 The Second Harmonic in Fluxgate Magnetometers . . . . .	8
2.1.3 Excitation Method of Ferromagnetic Cores . . . . .	10
2.2 Core Selection . . . . .	12
2.2.1 Toroidal Core Topology . . . . .	13
2.2.2 Core Material . . . . .	14
<b>3 Software Implementation</b>	<b>15</b>
3.1 Single-Core Topology . . . . .	16
3.2 Two-Core Topology . . . . .	20
3.3 Peripheral Expansion . . . . .	22
3.3.1 Synchronous Demodulator . . . . .	22
3.3.2 Low-Pass Filter . . . . .	24

## Contents

3.3.3	Voltage to Current Amplifier . . . . .	28
3.4	Closed-Loop Two-Core Topology . . . . .	31
3.5	Software Testing . . . . .	34
3.5.1	Maximum External Field Test . . . . .	34
3.5.2	Induced EMF Analysis . . . . .	36
3.5.3	Non-Ideal Testing . . . . .	40
<b>4</b>	<b>Hardware Implementation</b>	<b>44</b>
4.1	Circuit Schematic . . . . .	44
4.2	PCB Schematic . . . . .	47
4.3	Hardware Testing . . . . .	49
4.3.1	B-H Curve Test . . . . .	49
4.3.2	External Current Test . . . . .	53
<b>5</b>	<b>Discussion</b>	<b>57</b>
<b>6</b>	<b>Conclusion</b>	<b>63</b>
6.1	Further Work . . . . .	64
<b>References</b>		<b>66</b>

# List of Figures

1.1	Magnetic sensor comparison. . . . .	3
2.1	Typical B-H curve. . . . .	6
2.2	Drive waveforms in the time domain. . . . .	11
2.3	Drive waveforms in the frequency domain. . . . .	11
2.4	Fluxgate core geometry types. . . . .	12
2.5	Racetrack core. . . . .	12
2.6	Toroidal core topologies. . . . .	13
3.1	Flowchart process of fluxgate including peripherals. . . . .	15
3.2	Single-core drive and core design MATLAB implementation. . . . .	17
3.3	Single-core peripheral design MATLAB implementation. . . . .	17
3.4	LTspice circuit to visualize hysteresis. . . . .	18
3.5	B-H curve of Metglas MP2510 material. . . . .	19
3.6	Linearity test for single-core topology. . . . .	19
3.7	Two-core MATLAB core design. . . . .	20
3.8	Two-core MATLAB peripheral design. . . . .	21
3.9	Linearity test for two-core topology. . . . .	21
3.10	Synchronous demodulator MATLAB implementation. . . . .	23
3.11	Low-pass filter MATLAB implementation. . . . .	26
3.12	Low-pass filter LTspice implementation. . . . .	27
3.13	Bode plot of the designed filter. . . . .	27

## List of Figures

3.14	Voltage-Current amplifier MATLAB implementation.	29
3.15	Class B amplifier LTspice implementation.	30
3.16	Class B amplifier: $V_{in}$ and $I_{out}$ comparison.	31
3.17	Closed-loop two-core topology MATLAB implementation.	32
3.18	Closed-loop constant field test.	33
3.19	Closed-loop stepped field test.	34
3.20	Single-core open-loop maximum flux density test.	35
3.21	Two-core open-loop maximum flux density test.	35
3.22	Two-core closed-loop maximum flux density test.	36
3.23	Induced EMF waveforms of the two-core open-loop topology given $I_{ext} = 5 A$ .	37
3.24	Enhanced view of cancelled EMF waveform in open-loop topology.	37
3.25	Induced EMF waveforms of the two-core closed-loop topology given $I_{ext} = 5 A$ .	38
3.26	Enhanced view of cancelled EMF waveform in closed-loop topology.	39
3.27	Decision matrix for amplifier selection.	40
3.28	Peripheral circuitry LTspice implementation.	41
3.29	Output of non-ideal LTspice test.	42
3.30	$I_{comp}$ test between ideal and non-ideal conditions.	43
4.1	Input supply and mounting pins Fusion 360 implementation.	45
4.2	LTC1043 switched-capacitor Fusion 360 implementation.	45
4.3	Synchronous demodulator Fusion 360 implementation.	46
4.4	Buffer amplifier Fusion 360 implementation.	46
4.5	Sallen-key Fusion 360 implementation.	47
4.6	V-I amplifier Fusion 360 implementation.	47
4.7	Designed PCB (top).	48
4.8	Designed PCB (bottom).	49
4.9	B-H curve test setup schematic.	50
4.10	B-H curve test practical setup.	51
4.11	B-H curve test with sine wave drive excitation.	52

## List of Figures

4.12	B-H curve test with square wave drive excitation.	52
4.13	External current test setup schematic.	54
4.14	External current test practical setup.	55
4.15	External current test results.	56
5.1	Fluxgate AC field test.	58
5.2	Compensation winding test.	60
6.1	Three core fluxgate by Roland Bürger	65

## **List of Tables**

3.1	Simulation Parameters including Metglas MP2510 characteristics. . . . .	16
4.1	Summary of modules for B-H curve test. . . . .	50
4.2	Summary of modules for external current test. . . . .	53

# 1 Introduction & Motivation

Sensors play a critical role in modern electrical systems, serving as essential instruments that convert physical inputs into measurable outputs for real-time monitoring, control, and automation. The design of sensor technology must prioritise precision, efficiency, and reliability to meet the increasing demands of advanced electronic applications. Optimizing sensor characteristics such as bandwidth, energy efficiency, cost, and accuracy is fundamental to improving system performance. High-bandwidth sensors enable rapid data processing, which is crucial in dynamic environments such as power electronics, aerospace navigation, and autonomous systems. Energy efficient sensor designs reduce power consumption, a critical factor in battery powered space applications where energy resources are limited. Additionally, cost-effective sensors enhance scalability, making them viable for large scale deployment. As technology advances, the optimization of sensor systems remains pivotal in enhancing reliability, sustainability, and overall system efficiency.

Magnetic fields are fundamental forces of nature, present in planetary bodies, stellar formations, and even everyday household appliances. They also influence biological systems, such as the human brain [1]. These invisible magnetic fields play a critical role in a wide range of natural phenomena and technological applications, making magnetic field measurement essential across multiple disciplines. A magnetometer is an instrument used to measure magnetic field strength and direction. For over a century, magnetometers have contributed to scientific research and technological advancements, facilitating applications such as geophysical exploration, spacecraft navigation, and planetary research [2].

Early designs, such as Gauss' magnetometer, laid the foundation for modern magnetic sens-

## Chapter 1. Introduction & Motivation

ing technology. By the mid-20th century, advancements in electronics significantly enhanced the usability of magnetometers by reducing their size and cost, enabling their integration into aerospace, space exploration, and Earth observation missions [3] [4].

Supply Design Limited [5], established in 2001, specializes in the development of high-performance power conversion technology, with a strong focus on sustainability and transportation. The company collaborates with key aerospace industry leaders such as Raytheon, Clyde Space, and Umbra Group to drive technological innovation. In response to the growing adoption of superconducting devices within aerospace, which is driven by their electrical efficiency in cryogenic environments [6], Supply Design has shifted its focus toward developing robust measurement instruments capable of withstanding extreme environmental conditions. As part of this initiative, the company commissioned the development of a non-contact current sensor specifically designed for reliable operation in cryogenic environments.

Cryogenic conditions significantly alter the physical properties and performance of electronic components, affecting parameters such as on-resistance, switching speed, breakdown voltage, as well as voltage and current gain. As a result, careful consideration must be given during system design, and sensor performance must be optimised to ensure reliable operation under these extreme conditions. In the context of aerospace missions, electrical systems traditionally require extensive thermal insulation when operating in cryogenic environments, which adds weight, cost, and complexity. By directly integrating electrical systems into the cryogenic environment, these factors can be reduced, enabling more compact and lightweight designs [7] [8].

This project aligns with the United Nations Sustainable Development Goals (SDGs) [9] and the European Commission's strategy for achieving climate neutrality by 2050 [10]. Specifically, it contributes to SDG 9 (Industry, Innovation, and Infrastructure) and SDG 11 (Sustainable Cities and Communities) by promoting advancements in electrified transportation, including aircraft, aviation systems, and sustainable aerospace technologies. Furthermore, it aligns with the proposed SDG 18, Space Economy, which emphasizes the role of space-based technologies in driving economic growth and environmental sustainability. By incorporating electronic sys-

## Chapter 1. Introduction & Motivation

tems into these sectors, this project aims to reduce environmental impact and promote climate resilience as part of the broader transition toward a carbon-neutral economy.

In addition to its technological and environmental contributions, this project also promotes inclusivity and diversity by advancing sustainable air travel and commercial aviation solutions that benefit all individuals, regardless of gender, race, religion, or economic background.

Furthermore, ethical considerations are integral to the development of this project. All components are sourced exclusively from reputable suppliers that adhere to responsible, humane, and sustainable material sourcing practices.

The fluxgate magnetometer [11] was selected for this project due to its durability, low-cost fabrication, and broad range of detectable magnetic fields. Other magnetic sensing technologies, such as Hall effect magnetometers and SQUIDs (superconducting quantum interference devices) [12], offer distinct advantages in specific applications but do not match the fluxgate magnetometer's optimal combination of stability, sensitivity, and cost-effectiveness.

Figure 1.1 presents a comparison of various magnetometer technologies and their respective measurement ranges, illustrating the fluxgate's capability in magnetic field detection.

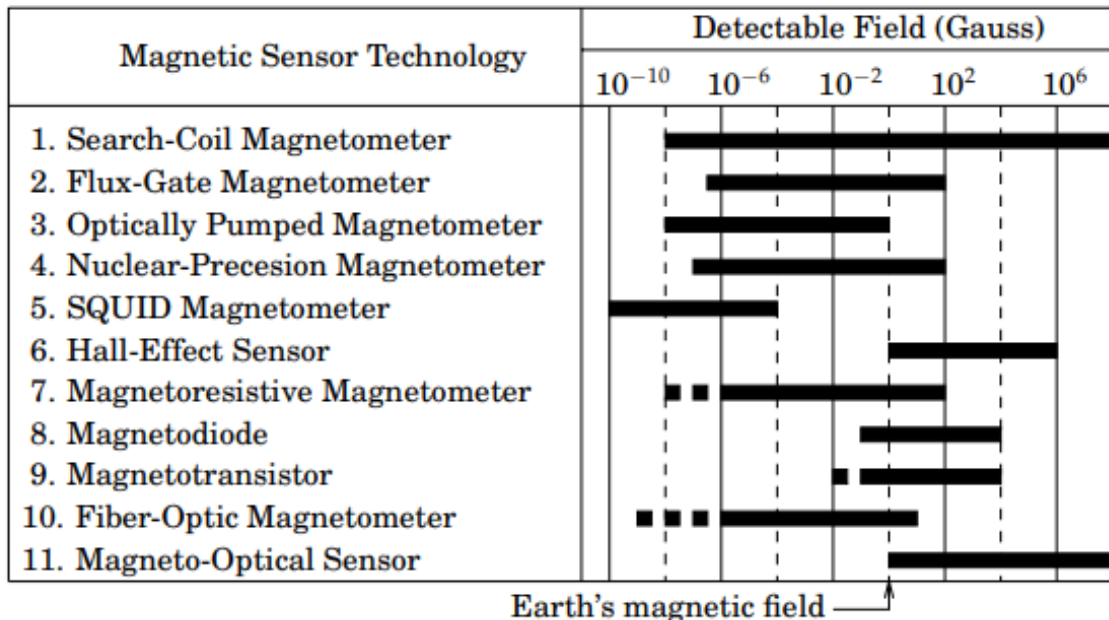


Figure 1.1: Magnetic sensor comparison [13]. Note:  $1T = 10^4G$ .

## Chapter 1. Introduction & Motivation

Fluxgate magnetometers are widely used in aerospace systems, primarily for magnetic field detection. A key application is in navigation, where attitude determination is achieved using three separate single-axis sensors aligned along the X, Y, and Z axes. These sensors enable accurate orientation tracking, which is essential for spacecraft trajectory control [14]. Fluxgate sensors also play a critical role in magnetic field mapping in both planetary and interplanetary environments, contributing to scientific understanding of planetary magnetic field structures and their interactions with space weather phenomena such as solar flares, magnetic clouds, and geomagnetic storms [15] [16].

## 2 Literature Review

### 2.1 Fluxgate Operating Principle

The operation of a fluxgate magnetometer is based on a ferromagnetic core, wound with two coils: a drive (primary) coil and a sense (secondary) coil. The primary coil is excited with an Alternating Current (AC), periodically driving the core into magnetic saturation during each half-cycle. This periodic magnetization generates a changing magnetic flux, which induces an electromotive force (EMF) in the secondary coil.

In the absence of an external magnetic field, the core's saturation response remains symmetrical, and the induced EMF follows a predictable, periodic pattern. However, when an external magnetic field is present, it alters the symmetry of the core's saturation response, causing a distortion in the induced EMF. This distortion is generated in the form of even-harmonics, where the second-harmonic component can be extracted and processed to determine the magnitude and direction of the external magnetic field.

#### 2.1.1 Hysteresis in Ferromagnetic Cores

Hysteresis is an intrinsic property of ferromagnetic materials that describes the lag between the applied magnetic field intensity and the resulting magnetic flux density. This phenomenon occurs because the magnetization of the material does not immediately follow the applied field, resulting in a characteristic hysteresis loop (B-H curve), as illustrated in Figure 2.1.

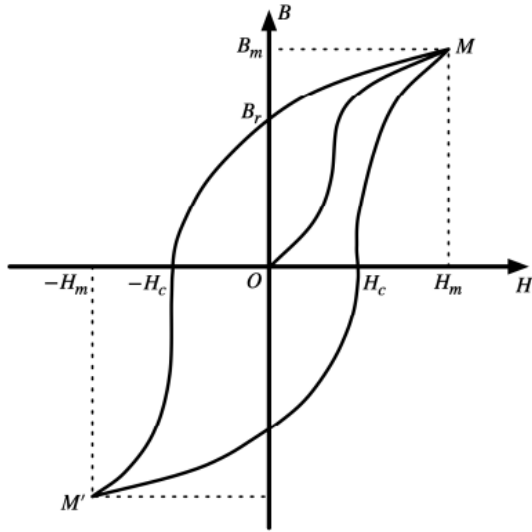


Figure 2.1: Typical B-H curve [17].

This curve defines the relative permeability of the core during a full saturation cycle and is calculated by:

$$\mu = \mu_0 \cdot \mu_r = \frac{B}{H} \quad (2.1)$$

- $\mu_0$ , Permeability of free space,  $4\pi \times 10^{-7} \frac{H}{m}$
- $\mu_r$ , Relative permeability of material, 1
- $B$ , Flux density, T
- $H$ , Field intensity,  $\frac{A}{m}$

As the magnetic field intensity increases, the relative permeability decreases as the material approaches magnetic saturation. This leads to weaker magnetic coupling between the applied field and the core, meaning further increases in the field intensity  $H$  produce smaller changes in magnetic flux density  $B$ . This behaviour can also be understood as an effective increase in magnetic reluctance as the core approaches saturation.

## Chapter 2. Literature Review

The fluxgate sensor measures external currents by detecting the resulting magnetic field intensity in its vicinity. This relationship is displayed through Ampère's Law:

$$H_{ext} = \frac{I_{ext}}{2\pi r} \quad (2.2)$$

- $I_{ext}$ , External current flowing through a conductor, A
- $r$ , Distance between the fluxgate sensor and external conductor, m

Since magnetic flux density is related to field intensity through the permeability:

$$B_{ext} = \mu H_{ext} \quad (2.3)$$

$$B_{ext} = \frac{\mu I_{ext}}{2\pi r} \quad (2.4)$$

This illustrates a fundamental principle of fluxgate operation. Specifically, that the external current can be inferred by detecting the magnetic flux density it produces in the sensor's vicinity.

The rate of change of  $B$ , which influences the induced EMF in a core, is given by Faraday's Law of Induction:

$$\varepsilon = N \frac{d\Phi}{dt} = N A_e \frac{dB}{dt} \quad (2.5)$$

- $\varepsilon$ , Induced EMF, V
- $N$ , Number of turns in the sense winding, turns
- $A_e$ , Cross-sectional area of a core,  $m^2$

In the presence of an external magnetic field  $B_{ext}$ , the induced EMF equation is modified as:

$$\varepsilon = N A_e \frac{d(B_{core} + B_{ext})}{dt} \quad (2.6)$$

## Chapter 2. Literature Review

In the presence of an external AC magnetic field, the continuously changing field directly influences the magnitude of the induced EMF. For an external Direct Current (DC) magnetic field, the field remains constant over time, so its time derivative is zero:

$$\frac{dB_{ext}}{dt} = 0 \quad (2.7)$$

This implies that the magnitude of the induced EMF remains unchanged. However, the presence of  $B_{ext}$  shifts the magnetization cycle of the core. This shift introduces an offset depending on the polarity and magnitude of  $B_{ext}$ , leading to even-harmonic distortion in the sensor's secondary winding.

### 2.1.2 The Second Harmonic in Fluxgate Magnetometers

Odd harmonics arise in the induced EMF due to the non-linear magnetization response (B–H curve) of a core. In contrast, even harmonics are generated when the periodic EMF waveform becomes asymmetrical.

In the case of a fluxgate magnetometer, the presence of an external magnetic field causes a skew in the magnetization cycle of the core material. This results in an asymmetric induced EMF waveform in the secondary coil. The distortion introduced by this asymmetry generates even harmonics, among which the second harmonic is the most dominant. Importantly, the amplitude of the second harmonic is directly proportional to the applied external magnetic field and can therefore be used as the measurable quantity to extract information about the external field.

The proportionality between the second-harmonic amplitude and the external magnetic field can be expressed as the product of the external flux density and a constant of proportionality:

$$A_2 \propto B_{ext} \quad (2.8)$$

$$\Rightarrow A_2 = k B_{ext} \quad (2.9)$$

## Chapter 2. Literature Review

- $k$ , Proportionality constant, 1
- $A_2$ , Amplitude of the second-harmonic frequency component,  $V$

Since the amplitude of the second harmonic is directly proportional to the strength of the external magnetic field, it serves as a key parameter in fluxgate sensor operation. This relationship can be represented as a Fourier series expansion:

$$\varepsilon(t) = A_1 \sin(\omega t) + A_2 \sin(2\omega t) + A_3 \sin(3\omega t) + \dots \quad (2.10)$$

- $A_1$ , Amplitude of the fundamental (drive) frequency component,  $V$
- $\omega$ , Angular frequency ( $2\pi f$ ),  $\frac{rad}{s}$

To extract the second-harmonic component from the induced EMF signal, the signal is multiplied by the second harmonic waveform,  $\sin(2\omega t)$ :

$$\varepsilon(t) \sin(2\omega t) = A_1 \sin(\omega t) \sin(2\omega t) + A_2 \sin(2\omega t) \sin(2\omega t) + \dots \quad (2.11)$$

Applying the trigonometric identity:

$$\sin(A) \sin(B) = \frac{1}{2} [\cos(A - B) - \cos(A + B)] \quad (2.12)$$

For the fundamental frequency component:

$$A_1 \sin(\omega t) \sin(2\omega t) = \frac{A_1}{2} [\cos(-\omega t) - \cos(3\omega t)] = \frac{A_1}{2} [\cos(\omega t) - \cos(3\omega t)] \quad (2.13)$$

When integrated over one full cycle  $T$ , both  $\cos(\omega t)$  and  $\cos(3\omega t)$  average to zero, eliminating the fundamental frequency contribution. For the second-harmonic component:

$$A_2 \sin(2\omega t) \sin(2\omega t) = \frac{A_2}{2} [\cos(0) - \cos(4\omega t)] = \frac{A_2}{2} [1 - \cos(4\omega t)] \quad (2.14)$$

## Chapter 2. Literature Review

Similarly,  $\cos(4\omega t)$  averages to zero. However the other term acts as a DC component, which averages to:

$$\frac{1}{T} \int_0^T \frac{A_2}{2} dt = \frac{A_2}{2} \quad (2.15)$$

For all higher harmonics, eq. 2.13 applies, meaning that when integrated over a full cycle, their contributions also average to zero. This derivation demonstrates that multiplying the signal by the second harmonic isolates the second-harmonic amplitude, while all other harmonic components vanish. The resulting value,  $\frac{A_2}{2}$ , directly correlates with the external magnetic field strength, allowing the signal information related to  $B_{ext}$  to be extracted provided the signal is effectively processed.

### 2.1.3 Excitation Method of Ferromagnetic Cores

An alternating drive signal is required to periodically drive the fluxgate core into and out of magnetic saturation. The excitation waveform can be a sinusoidal, square, or triangular wave, each ensuring symmetric core saturation in the absence of an external magnetic field. However, each waveform presents distinct advantages and disadvantages in terms of harmonic content and signal processing.

In terms of harmonics within the drive waveforms, a pure sinusoidal waveform consists of only its fundamental frequency component,  $\omega t$ , which ensures that the second-harmonic is the most dominant even harmonic in the induced EMF [18]. In contrast, triangular and square wave excitations contain multiple odd harmonics, with square waves exhibiting significantly higher harmonic content than triangular waves. This increased harmonic presence results in higher-order odd harmonics in the induced EMF, requiring extensive filtering to effectively extract the second-harmonic component. A visualization of each signal in the time domain and frequency domain is presented in Figure 2.2 and Figure 2.3.

## Chapter 2. Literature Review

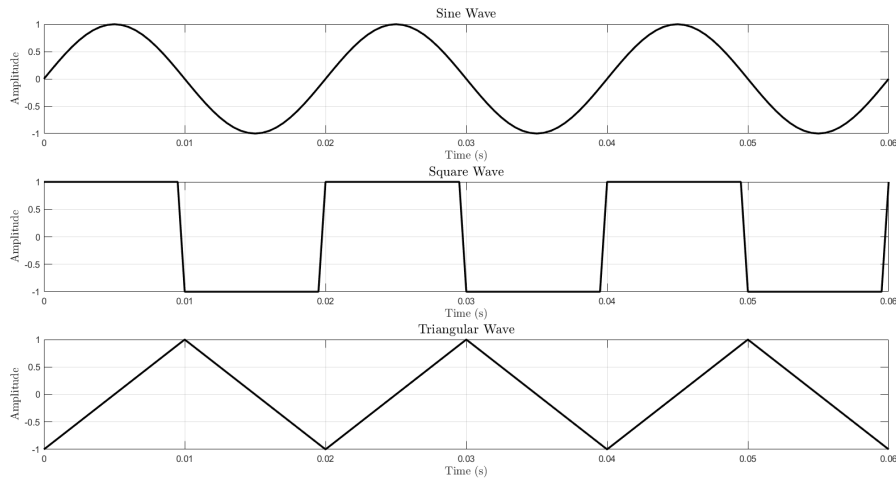


*Figure 2.2: Drive waveforms in the time domain.*

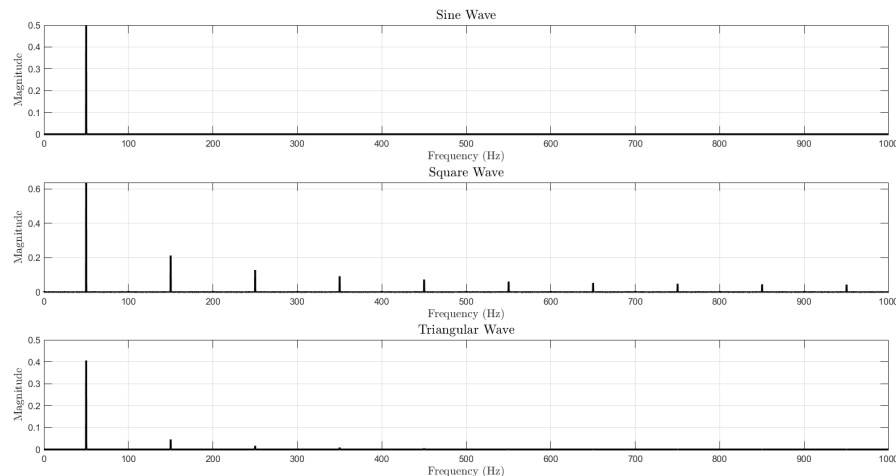


*Figure 2.3: Drive waveforms in the frequency domain.*

In terms of core magnetization, sinusoidal and triangular waveforms drive a ferromagnetic core into saturation gradually, requiring higher excitation currents to achieve full saturation. In contrast, a square wave excitation efficiently drives the core into saturation due to its abrupt transitions, minimizing the time spent in partial magnetization states.

From an implementation perspective, sinusoidal and triangular waveforms require greater circuit complexity, necessitating oscillators and additional peripherals such as integrators. Con-

versely, square wave excitation can be generated with minimal hardware, using Schmitt trigger circuitry or directly supplying the waveform from a microcontroller. Due to its efficiency in core saturation and ease of implementation, square wave excitation was chosen for this project, with the trade-off being the need for further filtering of the induced EMF signal to remove unwanted harmonics.

## 2.2 Core Selection

Historically, fluxgate core geometry has consisted of toroidal, rod, and tube-shaped designs, each with various winding methods, newer variations consist of designs such as racetrack cores. These configurations are illustrated in Figure 2.4 and Figure 2.5.

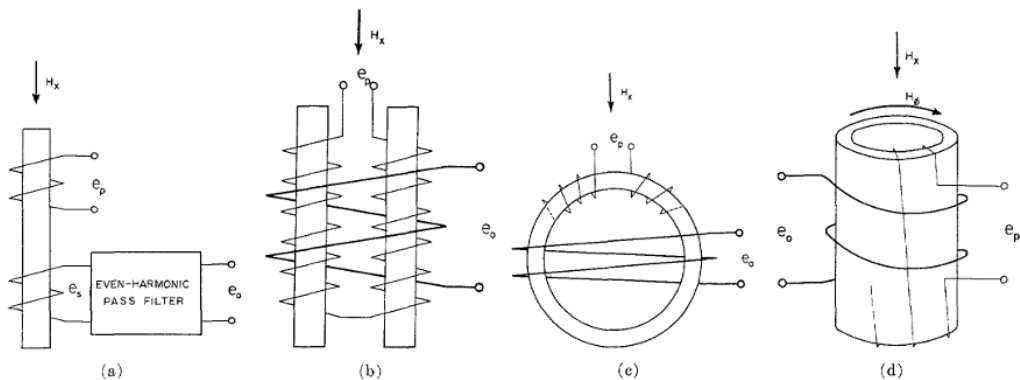


*Figure 2.4: Fluxgate core geometry types: (a) Single rod core, (b) Dual rod/Förster core, (c) Toroidal core, (d) Tube core [19].*

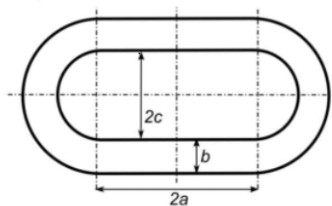


*Figure 2.5: Racetrack core [20].*

Toroidal cores are widely used in fluxgate magnetometers due to their closed magnetic path,

## Chapter 2. Literature Review

which minimizes flux leakage and enhances signal stability. This core geometry is also the most compact, making it suitable for a wide range of practical applications.

Rod and tube cores experience greater flux leakage due to their open-ended magnetic paths, leading to higher increased power requirements for full saturation [21].

Racetrack cores are less commonly used due to manufacturing challenges, as their elongated shape requires hand-wound coils. However, they require less drive power to reach saturation compared to rod and tube cores, making them a viable option for low-power applications [22].

The toroidal core topology was selected for this project due to its optimal balance between cost, efficiency and size.

### 2.2.1 Toroidal Core Topology

Among toroidal core fluxgate sensors, various expanded topologies incorporate multiple cores and specialized winding techniques [23]. The three primary configurations examined are illustrated in Figure 2.6.

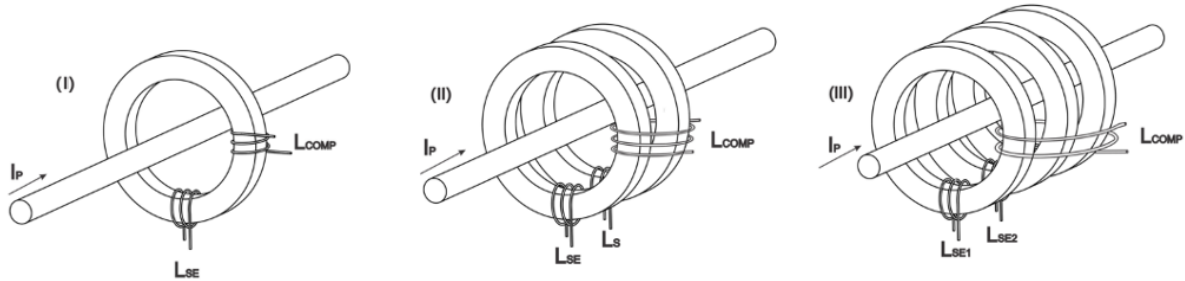


*Figure 2.6: Toroidal core topologies: (I) Single-core fluxgate, (II) Two-core fluxgate, (III) Three-core fluxgate [24].*

The single-core fluxgate features the simplest and most cost-effective design. However, this topology is prone to offset errors and exhibits lower sensitivity due to its operation in open-loop mode, which lacks feedback stabilization.

The two-core topology enhances the single-core design by incorporating an additional core wound in an anti-parallel configuration. This differential setup cancels odd harmonics, as their contributions are symmetric and out of phase in both cores. As a result, only even harmonics

## Chapter 2. Literature Review

remain which contain information relating to the external magnetic field. This effect leads to improved sensitivity and lower offset errors, making the two-core topology significantly more accurate and stable for magnetic field measurements.

The three-core topology incorporates an additional core that plays a critical role in enhancing bandwidth through high-frequency feedback. This third core becomes the dominant feedback path at higher frequencies, where the response of the conventional two-core system is insufficient to maintain accurate control [25].

Due to the increased complexity associated with the three-core fluxgate model, requiring elaborate control paths, this project focused on the design and implementation of a two-core fluxgate topology to ensure that development remains efficient and achievable within the time frame.

### 2.2.2 Core Material

The choice of core material is a critical factor in determining the performance, efficiency, and sensitivity of a fluxgate magnetometer. Common options include iron-based ferrite cores and advanced cobalt-based Metglas alloys, each offering distinct advantages based on their magnetic properties.

Ferrite cores, such as SIFERRIT T38 [26], provide a cost-effective solution with moderate permeability and saturation flux density, making them suitable for general-purpose applications. However, their lower permeability results in higher drive current requirements to achieve saturation, leading to increased core losses.

In contrast, Metglas alloys, such as MP2510 [27], are more expensive but offer significantly higher permeability, enhancing signal amplification, as described by  $B = \mu H$ . Alternatively this can be viewed as the reduction of drive current required for core saturation, as shown by the relationship  $H = \frac{NI}{l_e}$ , thereby lowering core losses and power consumption. Additionally, the increased permeability improves the magnetometer's ability to detect slight variations in external magnetic fields, resulting in enhanced resolution. These properties make Metglas the better core material for the fluxgate sensor.

### 3 Software Implementation

The software design of the fluxgate sensor involved several iterative modelling stages, with each model building upon the insights gained from the previous version. The final design, which was ultimately implemented in hardware, consists of a two-core topology with a compensation winding to enable closed-loop operation. A flowchart representation of the complete fluxgate system and its associated peripheral circuitry is provided in Figure 3.1.

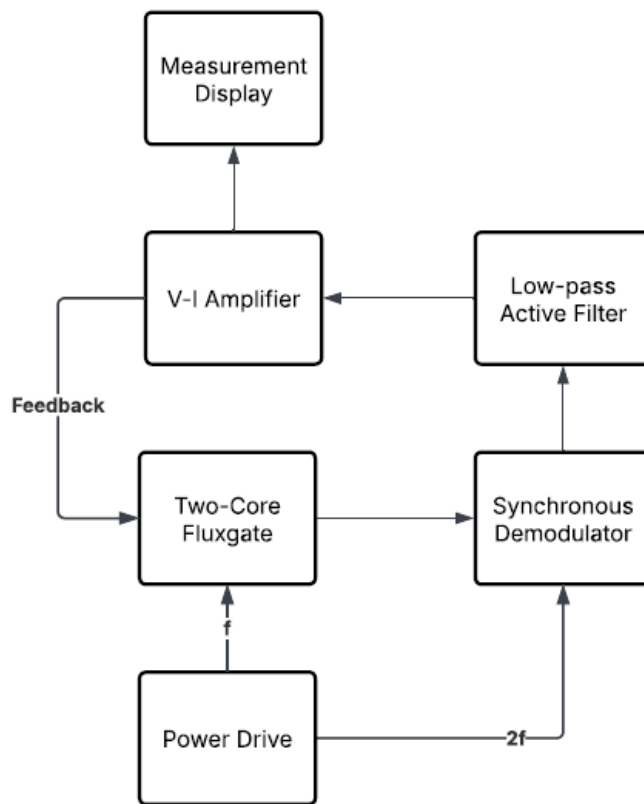


Figure 3.1: Flowchart process of fluxgate including peripherals.

### Chapter 3. Software Implementation

The purpose of the power drive is to periodically saturate the Metglas cores, inducing an EMF in the sense coil. The second harmonic of the drive frequency is extracted using a synchronous demodulator. This signal is then passed through a low-pass filter to isolate the DC component, which is directly proportional to the external magnetic field. The resulting signal is subsequently converted to a current and fed into the compensation winding, generating a magnetic field that actively cancels the external field. The magnitude of the feedback current is directly proportional to the original external field, enabling precise determination of the corresponding current amplitude.

Key parameters used for design simulations, containing Metglas characteristics, drive voltage, and current, are summarized in Table 3.1.

*Table 3.1: Simulation Parameters including Metglas MP2510 characteristics.*

Parameter	Definition	Value
$V_D$	Drive Voltage	10 V
$I_D$	Drive Current	5 A
$f_g$	Drive Frequency	25 kHz
$B_{sat}$	Saturation Flux Density	0.57 T
$\mu_r$	Relative Permeability	$100 \times 10^3$
$A_e$	Cross-sectional Area	$0.25 \text{ cm}^2$
$l_e$	Mean Flux Path Length	7.078 cm

To verify the feasibility and performance of the fluxgate topology before hardware implementation, a simulation-based approach was adopted, starting with a single-core fluxgate model before expanding to the two-core configuration.

### 3.1 Single-Core Topology

Initially, a high-level single-core design was implemented in MATLAB/Simulink as a foundational model, providing the basis for developing the more advanced two-core topology. A representation of the drive voltage and single-core setup is shown in Figure 3.2, while the corresponding simulation of the peripherals is illustrated in Figure 3.3.

### Chapter 3. Software Implementation

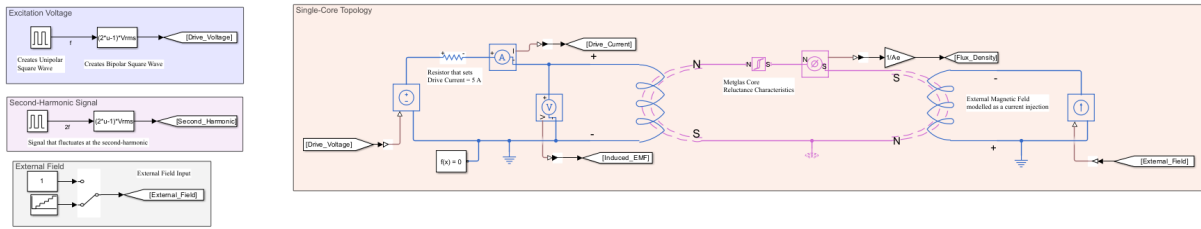


Figure 3.2: Single-core drive and core design MATLAB implementation.

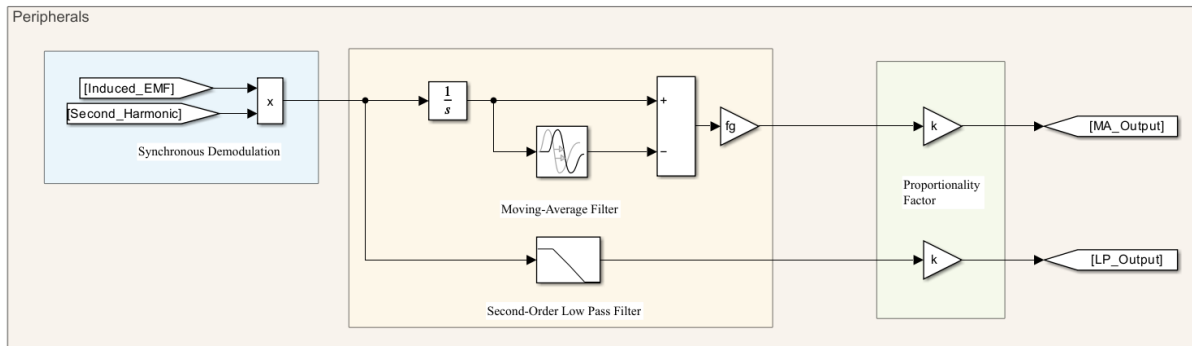


Figure 3.3: Single-core peripheral design MATLAB implementation.

The drive waveform is generated as a pulse waveform with a duty cycle of 50% between 0 and  $V_D$  at the frequency  $f_g$ . A function block is used to create a bipolar waveform ranging from  $-V_D$  to  $V_D$ . This waveform is incorporated into a multi-domain circuit that includes a current-limiting resistor to ensure the drive current is limited to  $I_D$ . The Metglas saturation characteristics are implemented using a non-linear reluctance block under single-point saturation, while the external field is modelled as a DC current source coupled to the core in reverse polarity to prevent measurement errors and slow simulations. Consequently, the polarity of the measured field in these simulations is reversed relative to the input. The external field is supplied either as a constant value or as a staircase function, allowing for evenly spaced increments during testing.

The peripherals section computes the functionality of the synchronous demodulator by taking the product of the induced EMF and the second-harmonic waveform. The resulting signal is filtered using both a low-pass filter and a moving average filter [28] for comparison. After the filtering stage, the waveform is multiplied by a proportionality factor determined through

### Chapter 3. Software Implementation

testing. The importance of this stage is maintaining linearity in the output across a range of external field inputs, whereas the proportionality factor itself is less critical, as it may vary under non-ideal conditions.

The B-H curve of the Metglas core can be obtained by plotting the drive current against the flux density. Under single-point saturation, the core is immediately driven into saturation, producing an idealized B-H curve. To further illustrate the hysteresis characteristics of the Metglas core, an LTspice circuit was designed, incorporating the core's magnetic properties. This circuit is shown in Figure 3.4.

A comparison between the single-point saturation model and the LTspice implementation of the hysteresis curve is presented in Figure 3.5. This data confirms that the applied drive current is sufficient to fully saturate the Metglas core and verifies that the unsaturated relative permeability of the core is:  $\mu_r \approx 100 \times 10^3$ .

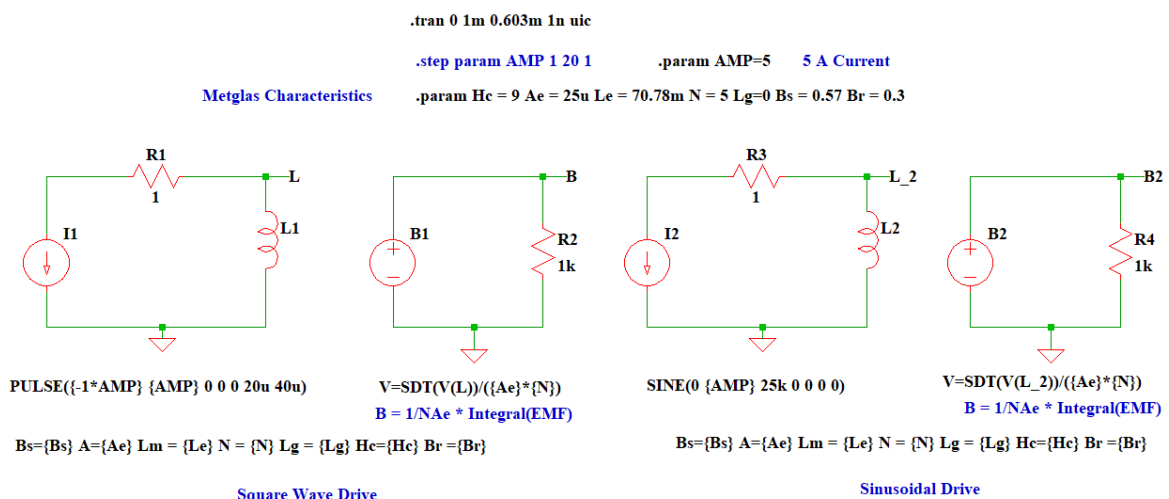


Figure 3.4: LTspice circuit to visualize hysteresis.

### Chapter 3. Software Implementation

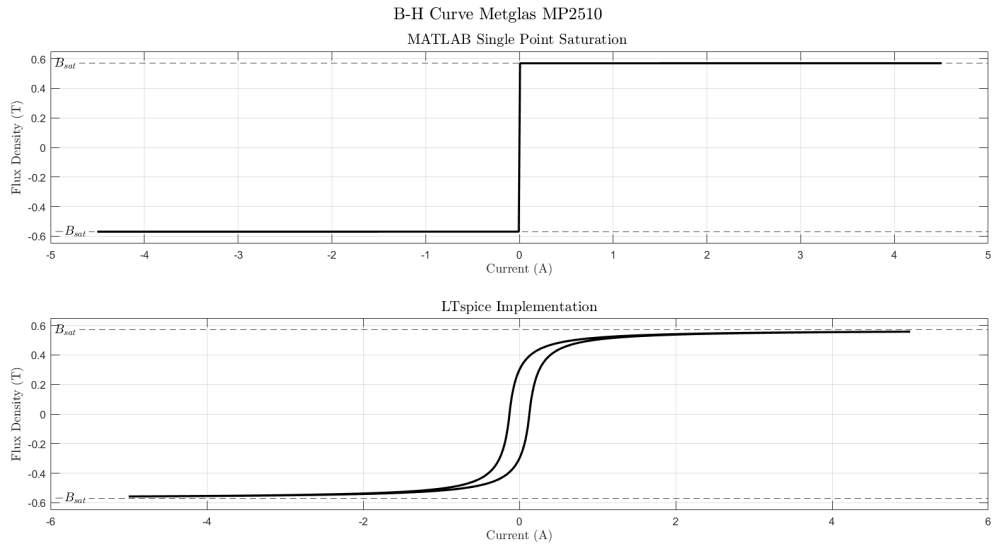


Figure 3.5: B-H curve of Metglas MP2510 material.

To evaluate the linearity of the fluxgate sensor output, a test was conducted by observing the response of the filter stage under a range of stepped external field parameters. The output was analysed to determine the consistency of its amplitude in response to the applied magnetic field. The test results are presented in Figure 3.6.

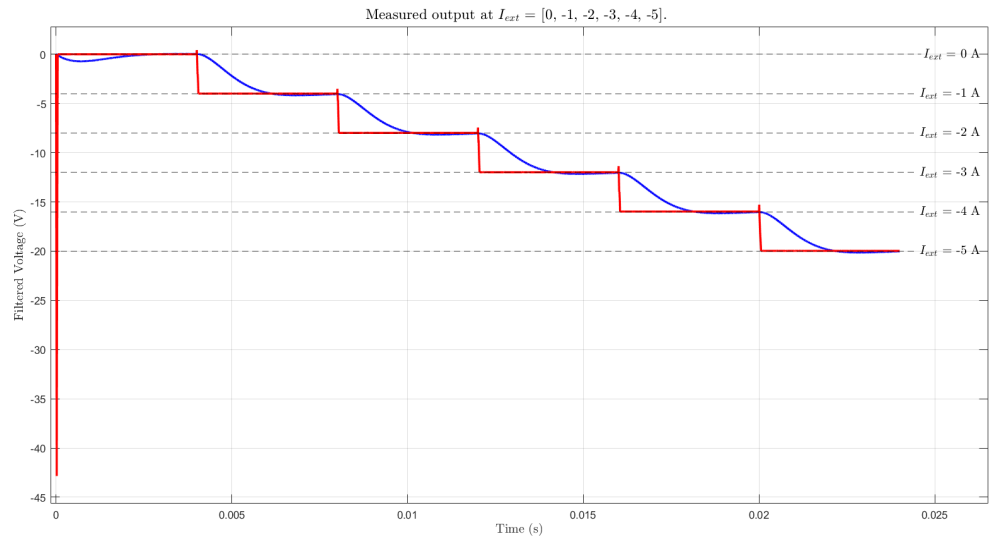


Figure 3.6: Linearity test for single-core topology.

## Chapter 3. Software Implementation

The data demonstrates that the output scales linearly with external field injection, as expected. The proportionality factor in this topology is determined to be  $k = \frac{1}{4}$ .

### 3.2 Two-Core Topology

As stated previously, the two-core topology incorporates a second toroidal Metglas core with identical characteristics to the first. The key distinction is that the second core is wound in an anti-parallel configuration relative to the first core. This configuration results in an induced EMF that cancels out the symmetrical components of the signal, preserving only the components generated by even harmonics. The peripheral design includes an additional element that models the cancellation of the induced EMF signals through an addition block.

A representation of the core circuitry of the two-core topology is shown in Figure 3.7, along with the corresponding peripheral section depicted in Figure 3.8. The drive circuitry for this model remains the same as the single-core topology seen in Figure 3.2.

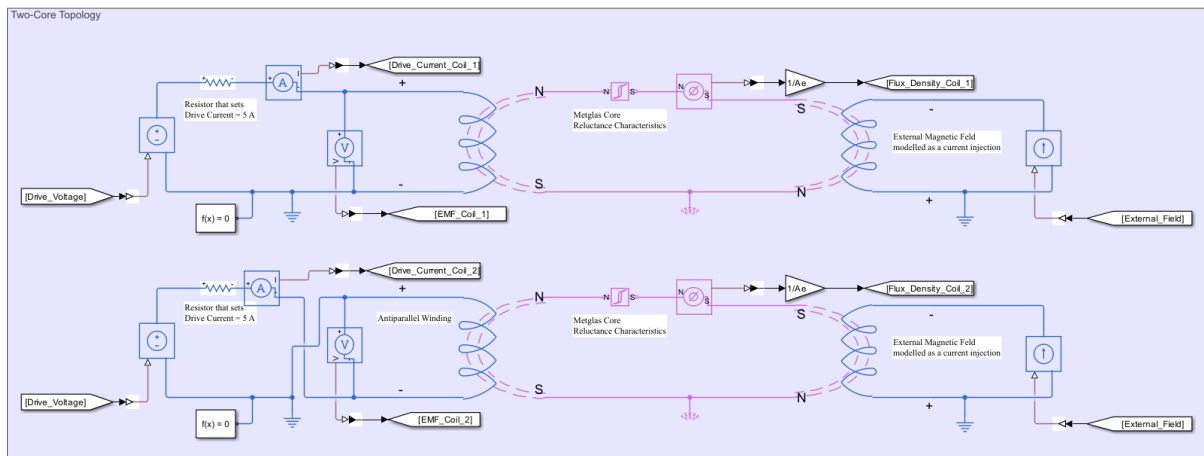


Figure 3.7: Two-core MATLAB core design.

### Chapter 3. Software Implementation

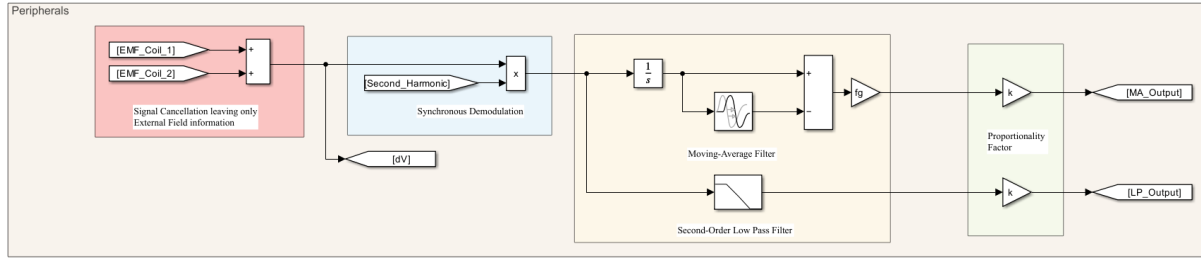


Figure 3.8: Two-core MATLAB peripheral design.

After conducting a linearity test on the two-core fluxgate sensor, it was found that the proportionality factor was doubled for this specific circuit,  $k = \frac{1}{8}$ . The results of the test are presented in Figure 3.9.

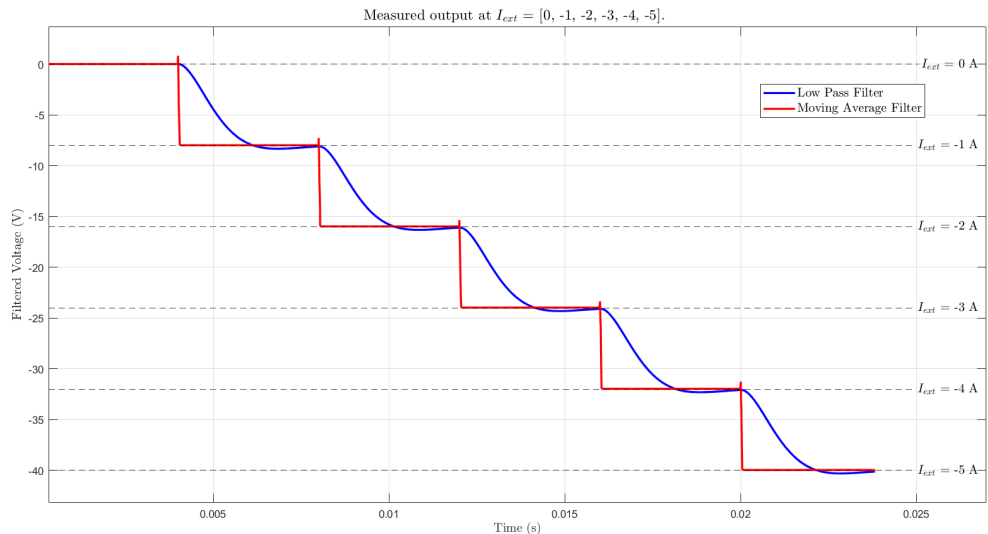


Figure 3.9: Linearity test for two-core topology.

The reason behind this two-fold output is due to the introduction of the second core. The equations for the generated EMFs of each core,  $\varepsilon_1$  and  $\varepsilon_2$ , under no external field are described as:

$$\varepsilon_1(t) = A_1 \sin(\omega t) + A_3 \sin(3\omega t) + \dots \quad (3.1)$$

Remembering the second core is wound antiparallel:

$$\varepsilon_2(t) = -A_1 \sin(\omega t) - A_3 \sin(3\omega t) - \dots \quad (3.2)$$

The polarity of the even harmonics is dependent on the polarity of the external field so these equations become:

$$\varepsilon_1(t) = A_1 \sin(\omega t) + A_2 \sin(2\omega t) + A_3 \sin(3\omega t) + \dots \quad (3.3)$$

$$\varepsilon_2(t) = -A_1 \sin(\omega t) + A_2 \sin(2\omega t) - A_3 \sin(3\omega t) + \dots \quad (3.4)$$

The induced EMF is the sum of the induced EMF components:

$$\varepsilon(t) = \varepsilon_1(t) + \varepsilon_2(t) = 2A_2 \sin(2\omega t) \quad (3.5)$$

Following the same methodology outlined in equations 2.12–2.15, the result yields  $A_2$  instead of the single-core result  $\frac{A_2}{2}$ , thereby doubling the proportionality factor.

### 3.3 Peripheral Expansion

Within the single-core and two-core topologies, signal processing blocks were utilised in the peripherals section to convert the EMF signal into the corresponding current. For practical implementation, these peripherals must be translated into hardware circuits. Consequently, each peripheral, including the synchronous demodulator, second-order low-pass filter, and the voltage to current amplifier stage, must be replaced with practical circuit equivalents for hardware implementation.

#### 3.3.1 Synchronous Demodulator

The synchronous demodulator's purpose within the fluxgate sensor is to extract the second-harmonic component by multiplying the induced EMF signal with an external reference signal

### Chapter 3. Software Implementation

oscillating at the second-harmonic frequency. Several topologies can perform this operation, including digital synchronous demodulation, lock-in amplifiers, and switched-capacitor based demodulation.

For this design, a switched-capacitor synchronous demodulator was chosen due to its low cost, reduced circuit complexity, and minimal component count. Unlike digital synchronous demodulation, which offers high flexibility and accuracy, it requires significant processing power and an external FPGA for implementation. Similarly, while a lock-in amplifier is highly effective for low-noise applications, it demands a complex design with multiple components and additional peripherals, increasing both cost and implementation difficulty.

The switched-capacitor approach ensures effective synchronous demodulation while maintaining a compact and simple implementation. However, a key limitation of the switched-capacitor topology is its inability to detect phase information, resulting in the loss of critical data when measuring AC magnetic fields. This is particularly problematic for high-speed AC signals, where both amplitude and phase are essential for accurate measurement and analysis.

The implementation approach of the switched-capacitor synchronous demodulator was based on a reference design (Lock-In Amplifier) from the LTC1043 switched-capacitor datasheet [29]. This was modelled within Simulink and can be seen in Figure 3.10.

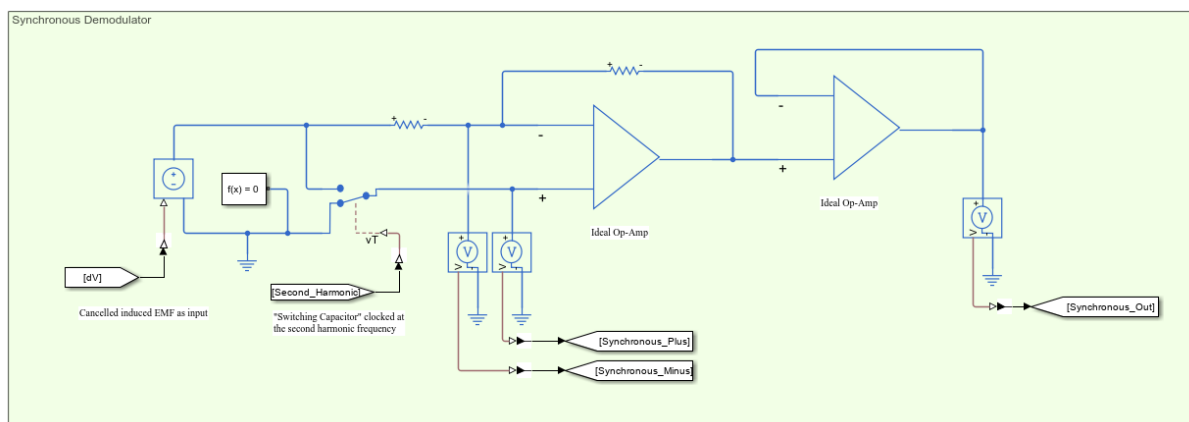


Figure 3.10: Synchronous demodulator MATLAB implementation.

This circuit takes the induced EMF after summation as its input. This signal is then fed into

### Chapter 3. Software Implementation

the negative terminal of an ideal operational amplifier with resistors  $R_f = R_1 = 10\text{ k}\Omega$ . As a result, the gain of this amplifier stage is  $G_V = -1$ .

Meanwhile, an ideal switch alternates between the induced EMF signal and ground at the second-harmonic frequency, effectively sampling the induced EMF at  $2\omega t$ . This process results in a multiplication of the induced EMF by a pulse waveform oscillating at  $2\omega t$ , which isolates the second-harmonic component. Finally this output travels through another ideal amplifier configured as a buffer and is directed to the filtering stage.

#### 3.3.2 Low-Pass Filter

The low-pass filter is required to extract the DC information ( $A_2$ ) from the second-harmonic signal. Since the desired output is a DC component, the cutoff frequency of this filter must be significantly lower than the fundamental frequency. The main topologies for this filter include passive filters utilising resistors, capacitors, and inductors, or active filters that incorporate an operational amplifier.

Passive filtering is a cost-effective approach with little complexity. However, it has a gain of less than unity, which can potentially affect the accuracy of the fluxgate through signal attenuation. While active filters require an external power source along with passive components, they offer improved stability and control through feedback. Given these advantages, an active filter was selected for this design to ensure reliable performance.

There are various topologies within active filters, including higher-order designs with Cheby-shev and Butterworth filter responses. For this design, a second-order Sallen-Key filter with a Butterworth response was implemented to ensure a maximally flat frequency response without ripple to maintain a stable output. The gain equation of a second-order low-pass Sallen-key filter is:

$$\frac{V_o}{V_{in}} = \frac{Z_3 Z_4}{Z_1(Z_2 + Z_4) + Z_4(Z_2 + Z_3)} \quad (3.6)$$

Substituting  $Z_1 = R_1$ ,  $Z_2 = R_2$ ,  $Z_3 = \frac{1}{sC_3}$ , and  $Z_4 = \frac{1}{sC_4}$  gives the equation:

### Chapter 3. Software Implementation

$$\frac{V_o}{V_{in}} = \frac{1}{s^2 R_1 R_2 C_3 C_4 + s C_3 (R_1 + R_2) + 1} \quad (3.7)$$

For a second-order Butterworth filter, the normalised transfer function [30] is given by:

$$\frac{V_o}{V_{in}} = \frac{1}{s^2 + 1.414s + 1} \quad (3.8)$$

Equating the Laplace coefficients gives:

$$R_1 R_2 C_3 C_4 = 1 \quad (3.9)$$

and

$$C_3 (R_1 + R_2) = 1.414 \quad (3.10)$$

Firstly setting  $R_1 = R_2 = 1 \Omega$ , allows the calculation of  $C_3$  and  $C_4$ :

$$C_3 = \frac{1.414}{(R_1 + R_2)} = \frac{1.414}{2} = 0.707 F \quad (3.11)$$

$$C_4 = \frac{1}{R_1 R_2 C_3} = \frac{1}{1 \times 1 \times 0.707} = 1.414 F \quad (3.12)$$

For practical implementation frequency scaling is required with the factor:

$$\omega_c = 2\pi f_c = 2\pi \times 250 \quad (3.13)$$

$C_3$  and  $C_4$  now become:

$$C_3 = \frac{0.707}{2\pi f_c} = \frac{0.707}{2\pi \times 250} = 450 \mu F \quad (3.14)$$

$$C_4 = \frac{1.414}{2\pi f_c} = \frac{1.414}{2\pi \times 250} = 900 \mu F \quad (3.15)$$

### Chapter 3. Software Implementation

Magnitude scaling is also required, using a factor  $\rho = 10 \times 10^3$ , the component values become:

$$R_1 = R_2 = \rho = 10 \text{ } k\Omega \quad (3.16)$$

$$C_3 = \frac{450 \times 10^{-6}}{\rho} = \frac{450 \times 10^{-6}}{10 \times 10^3} = 45 \text{ } nF \quad (3.17)$$

$$C_4 = \frac{900 \times 10^{-6}}{\rho} = \frac{900 \times 10^{-6}}{10 \times 10^3} = 90 \text{ } nF \quad (3.18)$$

A MATLAB implementation of this filter is shown in Figure 3.11 as well as an LTspice implementation to create a bode plot depicting the frequency response of the filter, the circuit is shown in Figure 3.12 as well as the resulting bode plot in Figure 3.13.

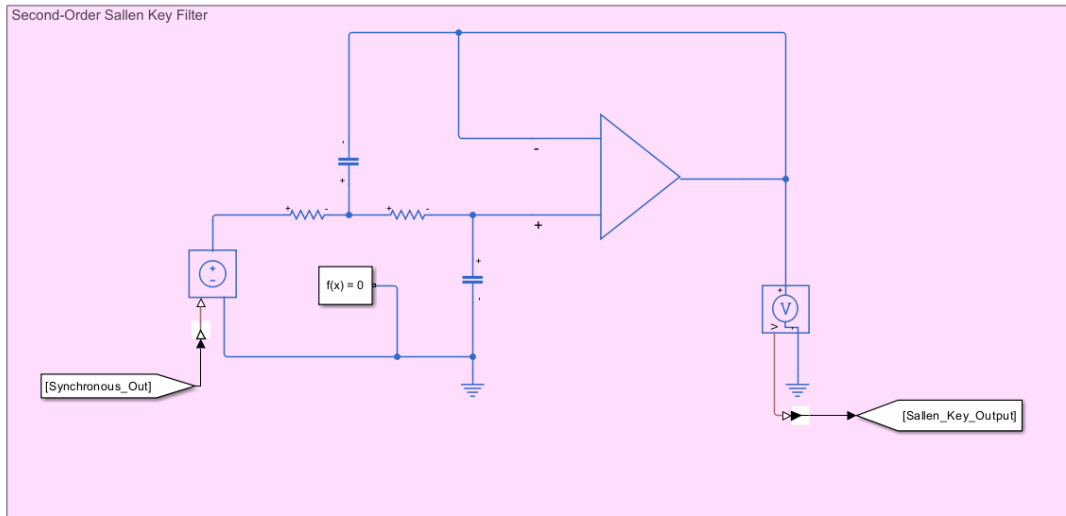


Figure 3.11: Low-pass filter MATLAB implementation.

### Chapter 3. Software Implementation

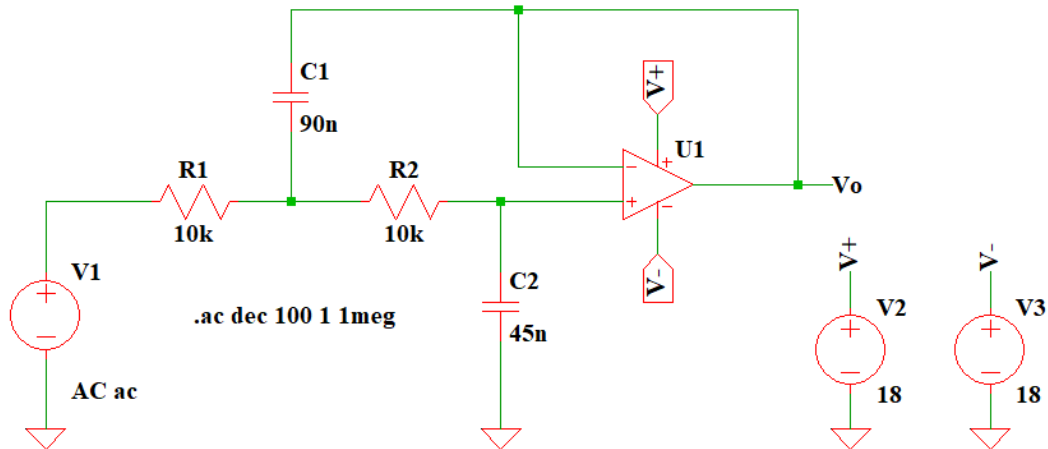


Figure 3.12: Low-pass filter LTspice implementation.

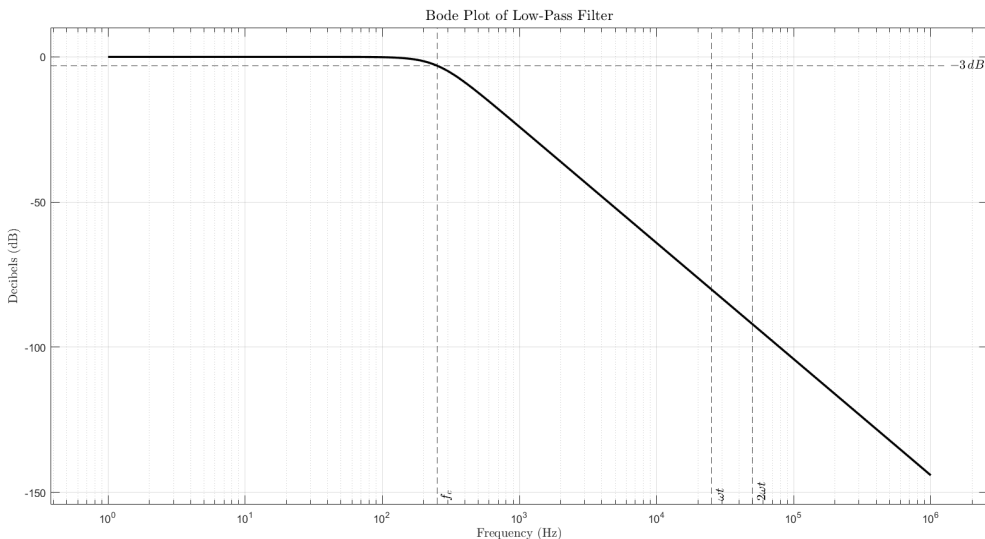


Figure 3.13: Bode plot of the designed filter.

This plot demonstrates that the cutoff frequency of the active filter aligns well with the intended design specification. Additionally, it highlights that for frequencies at and beyond  $f_g$ , the filter exhibits significant attenuation, exceeding  $-70$  dB. This suppression indicates that the filter is able to isolate the DC component of the external magnetic field, ensuring minimal distortion in its output.

### 3.3.3 Voltage to Current Amplifier

The final stage of this instrument incorporates a voltage to current amplifier. The purpose of this amplifier is to convert the extracted DC component of the EMF signal into current. This current can then be fed back into the core via a compensation winding, closing the loop of the system and nullifying the distortion caused by the external field. This enhances the accuracy of the instrument as it remains in a near-zero field condition due to its active feedback. In principle, the magnitude of the compensation current provides a direct proportional measurement to the external field. Topologies for this peripheral include operational transconductance amplifiers, Class B push-pull amplifiers and Class A amplifiers.

Operational transconductance amplifiers (OTAs) offer low power consumption; however, they have limited output current capability [31] compared to Class A and Class B stages [32]. Among these, Class B stages are more power-efficient than Class A, whilst maintaining the ability to convert voltage to current for both positive and negative input signals. However, a common drawback of Class B amplifiers is crossover distortion, which occurs when both transistors remain off near zero input, leading to signal loss.

In the case of a fluxgate sensor, a DC field ensures that the input to this peripheral remains either entirely positive or entirely negative, in the case of an AC field the buffer amplifier with feedback helps eliminate the issue of this crossover distortion. For this reason, a Darlington Class B amplifier was chosen for this design to maximize current output while maintaining efficiency.

The implementation of this peripheral in MATLAB is shown in Figure 3.14, consisting of a buffer amplifier with feedback, followed by the Darlington Class B amplifier.

### Chapter 3. Software Implementation

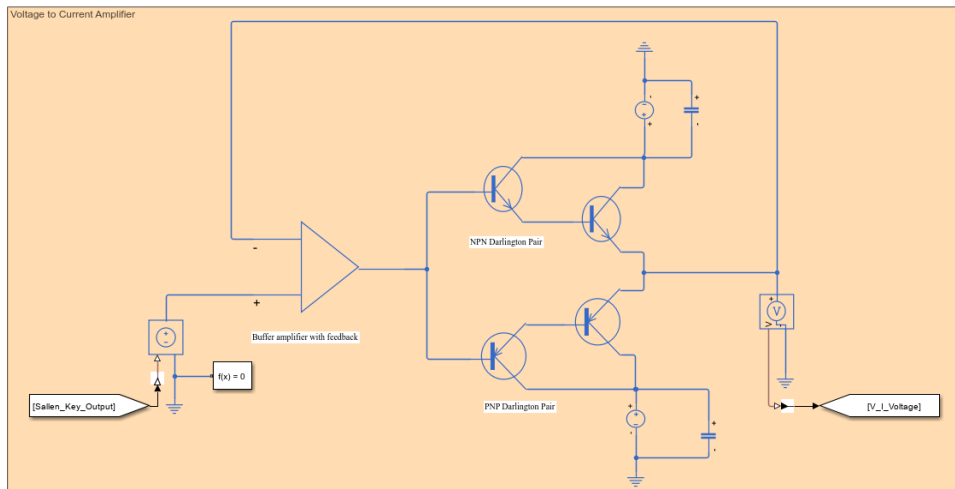
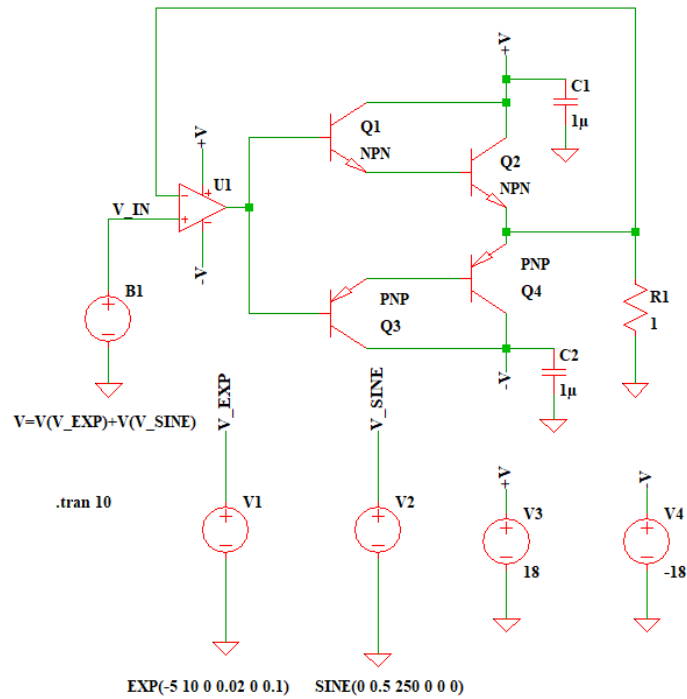


Figure 3.14: Voltage-Current amplifier MATLAB implementation.

Within MATLAB, the circuit exhibits inconsistencies between the output voltage and output current, where the current remains near zero. To address this issue, an LTspice implementation was developed using a test input to verify the voltage-to-current conversion before integrating it into closed-loop topology. The test circuit can be seen within Figure 3.15.

### Chapter 3. Software Implementation



*Figure 3.15: Class B amplifier LTspice implementation.*

The circuit was given a test input consisting of an exponential signal that steady states at  $-5\text{ V}$ . Superimposed on this was a sinusoidal wave with a small amplitude to act as distortion within the exponential signal. The input voltage and the output current waveforms can be seen in Figure 3.16.

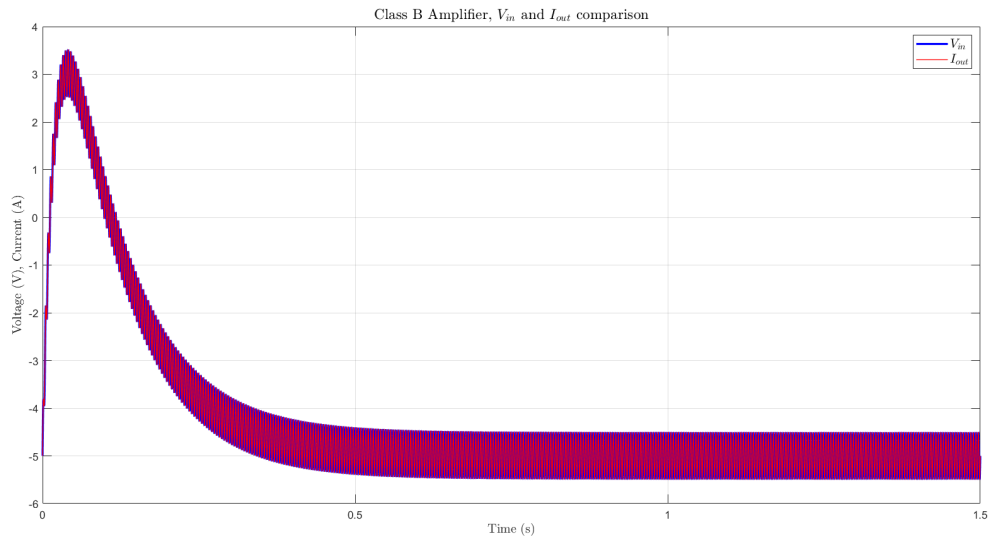


*Figure 3.16: Class B amplifier:  $V_{in}$  and  $I_{out}$  comparison.*

The data confirms that the output current follows the input voltage, validating the voltage-to-current conversion in LTspice. To resolve the discrepancy in MATLAB, the voltage output was used for the closed-loop topology.

### 3.4 Closed-Loop Two-Core Topology

The closed-loop two-core topology requires the implementation of feedback via a compensation winding. The input to this compensation winding is the output of the V-I amplifier, which passes through both cores and is connected to a grounded resistor. Over time, this feedback mechanism nullifies the distortion caused by the external magnetic field, ensuring accurate field compensation. The implementation of this closed-loop topology can be seen in Figure 3.17.

### Chapter 3. Software Implementation

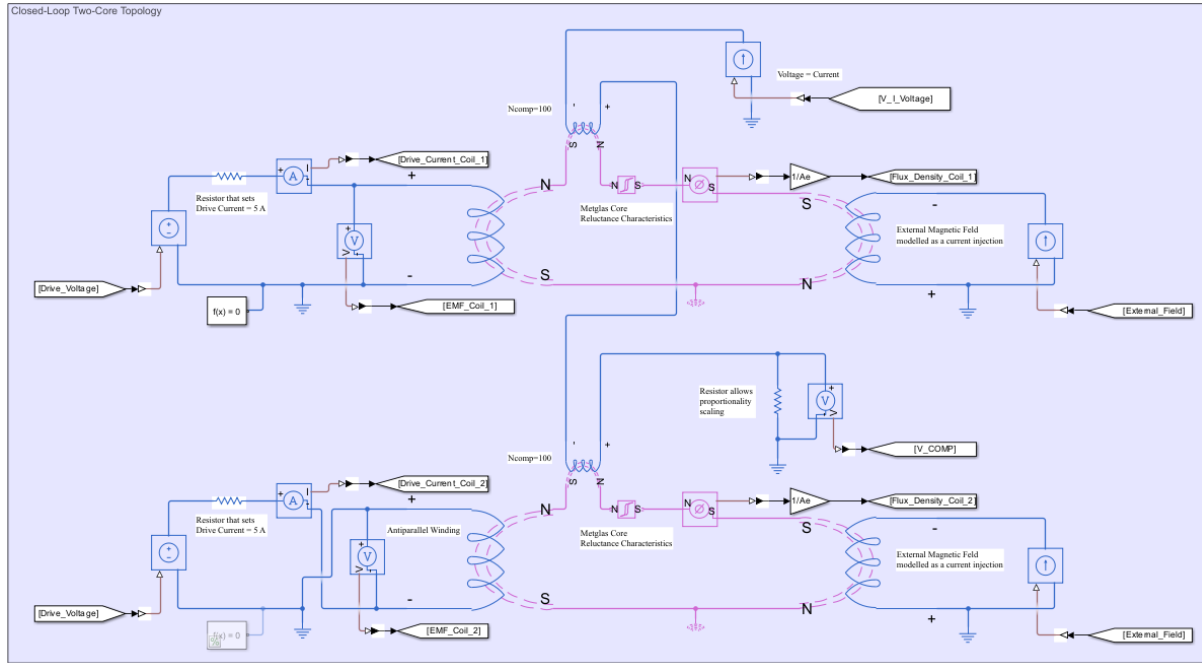


Figure 3.17: Closed-loop two-core topology MATLAB implementation.

The mathematical representation of the two core functionality begins with assuming effective field cancellation meaning the magnetomotive force of the external field and the compensation winding are equal:

$$\mathcal{F}_{comp} = \mathcal{F}_{ext} \quad (3.19)$$

$$N_{comp}I_{comp} = N_{ext}I_{ext} \quad (3.20)$$

However  $N_{ext} = 1$ :

$$I_{comp} = \frac{I_{ext}}{N_{comp}} \quad (3.21)$$

At this point, the proportionality between the compensation current and the external field current is evident. Given that  $I_{comp}$  flows through the grounded resistor  $R_{comp}$ , the voltage is:

### Chapter 3. Software Implementation

$$V_{comp} = I_{comp}R_{comp} = \frac{I_{ext}R_{comp}}{N_{comp}} \quad (3.22)$$

By selecting the resistor value equal to the number of compensation turns ( $R_{comp} = N_{comp}$ ), the measured voltage directly corresponds to the magnitude and polarity of the external field current:

$$V_{comp} = \frac{I_{ext}R_{comp}}{R_{comp}} = I_{ext} \quad (3.23)$$

To verify this approach, a test was conducted with  $N_{comp} = R_{comp} = 100$  to ensure proper operation. The results are presented in Figures 3.18 and 3.19. Under this condition, the accuracy of the fluxgate sensor was determined to be  $\eta = 98.8\%$ , and it is shown that the system demonstrates consistent linearity.

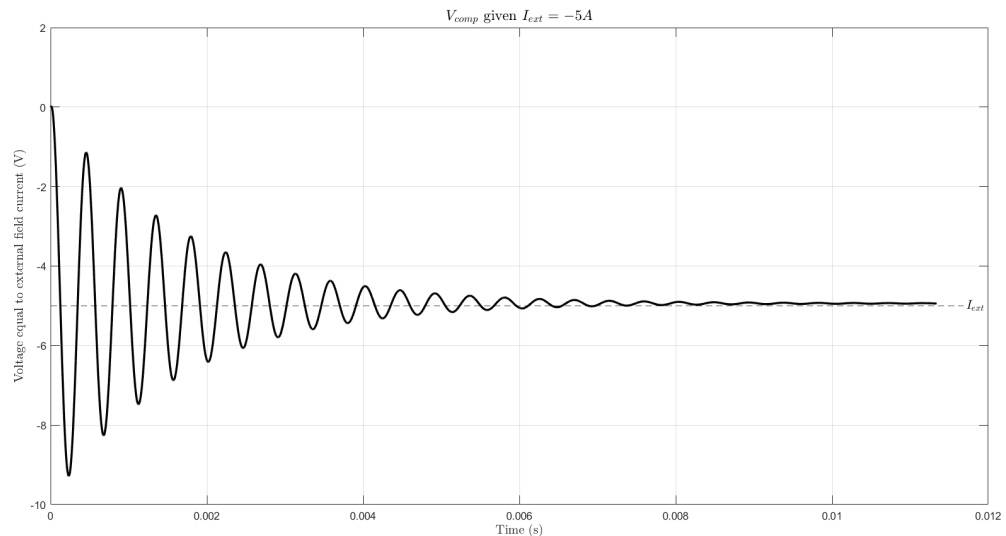


*Figure 3.18: Closed-loop constant field test.*

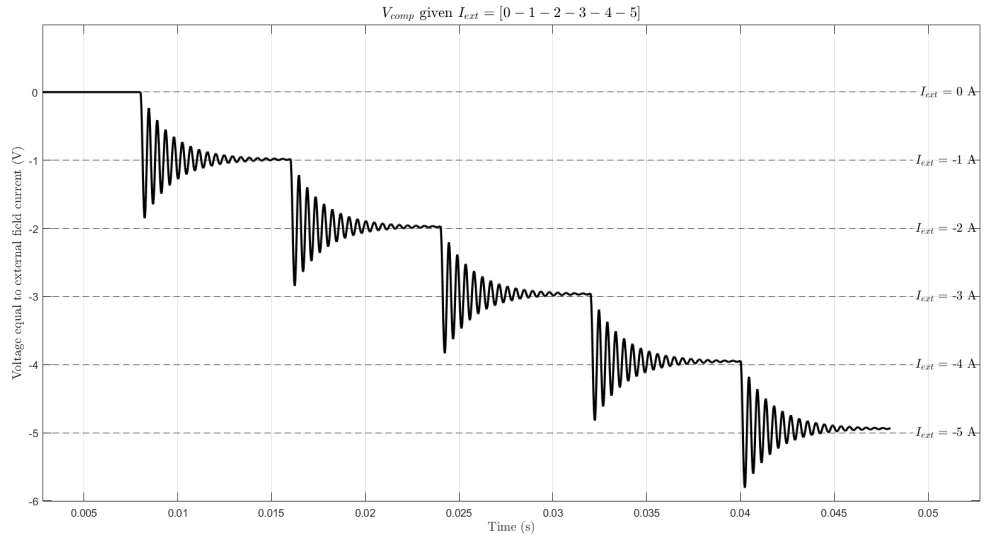


*Figure 3.19: Closed-loop stepped field test.*

## 3.5 Software Testing

With the completion of a working fluxgate model operating in closed-loop, the next step was to introduce testing with non-ideal components in order to evaluate the practical limitations of the system. This phase of testing aimed to identify the critical component characteristics required for proper operation, including maximum voltage supply requirements, amplifier slew rates, and other non-ideal behaviours that could degrade the sensor's accuracy through information loss.

### 3.5.1 Maximum External Field Test

The first set of tests focused on determining the maximum external field that can be reliably measured. This was assessed by incrementally increasing the external field current until the core(s) no longer reached magnetic saturation in both the positive and negative directions. The resulting flux behaviour for the single-core configuration, as well as for the two-core topology in both open- and closed-loop operation, is shown in Figures 3.20 - 3.22.

### Chapter 3. Software Implementation

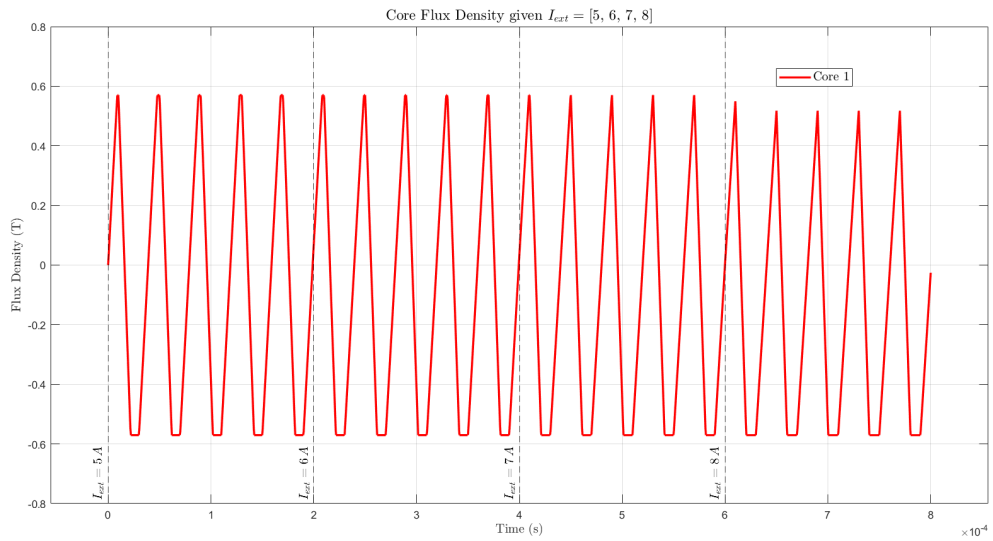


Figure 3.20: Single-core open-loop maximum flux density test.

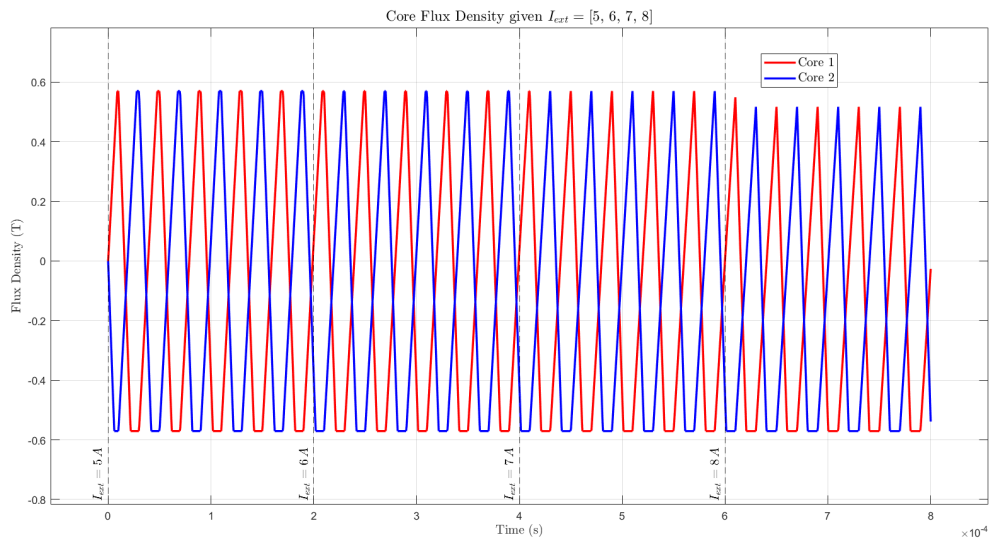
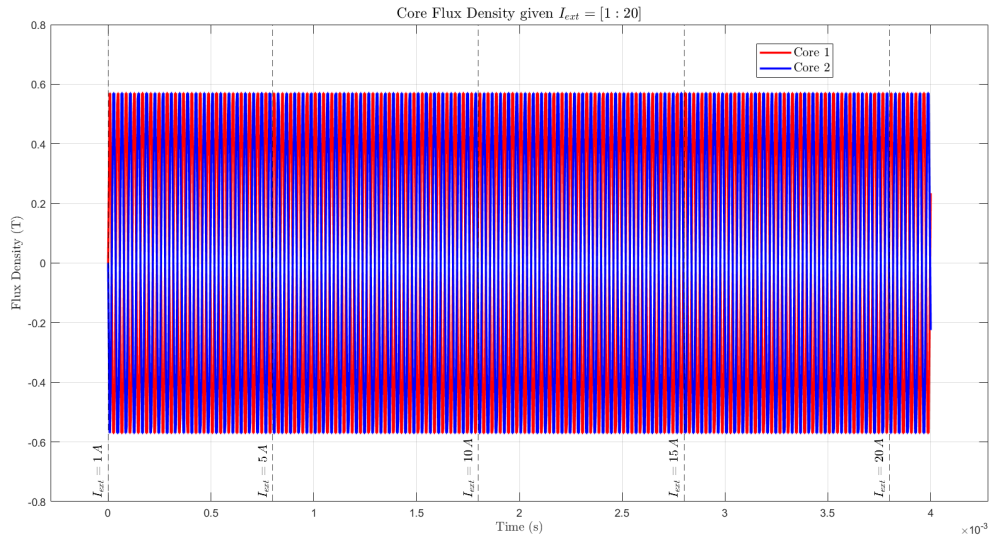


Figure 3.21: Two-core open-loop maximum flux density test.



*Figure 3.22: Two-core closed-loop maximum flux density test.*

The results show that for an external current exceeding  $I_{ext} = 8 A$ , the cores are no longer driven into saturation in the open-loop scenarios. However, due to the added control provided by the feedback in the closed-loop system, the simulation demonstrates that with incremental increases in external current, the closed-loop configuration is capable of handling significantly higher values without loss of functionality. For consistency and control throughout the remainder of the project, an upper limit of  $I_{ext} = 5 A$  was defined.

### 3.5.2 Induced EMF Analysis

With the upper limit of  $I_{ext} = 5 A$  now defined, the next step is to analyse the induced EMF waveform that serves as the input to the peripherals. This analysis is carried out to characterise the waveform's minimum and maximum voltage levels, as well as to determine the slew rate requirements necessary to ensure fluxgate performance. The corresponding EMF waveforms, both before and after cancellation, are shown in Figure 3.23 along with an in depth view of the cancelled EMF waveform in Figure 3.24.

### Chapter 3. Software Implementation

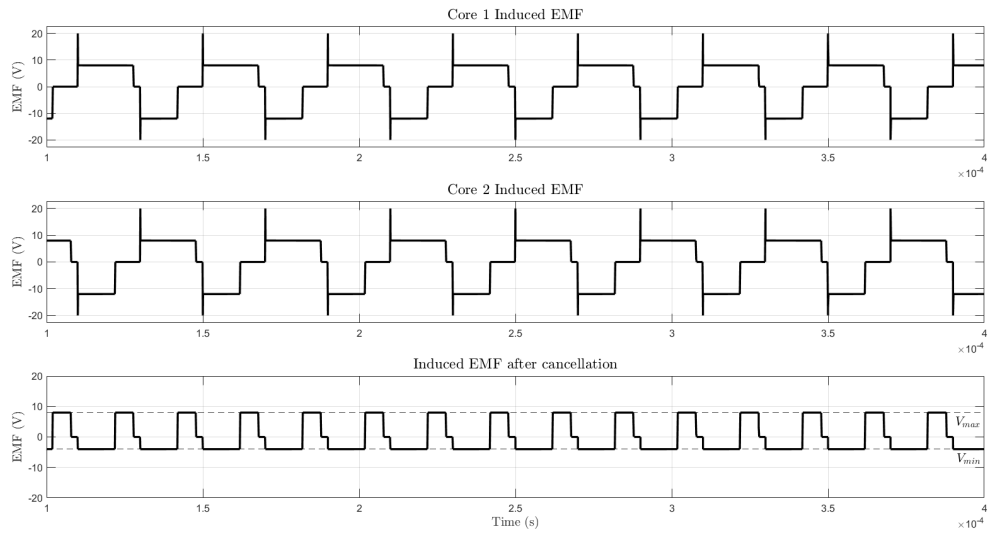


*Figure 3.23: Induced EMF waveforms of the two-core open-loop topology given  $I_{ext} = 5 A$ .*

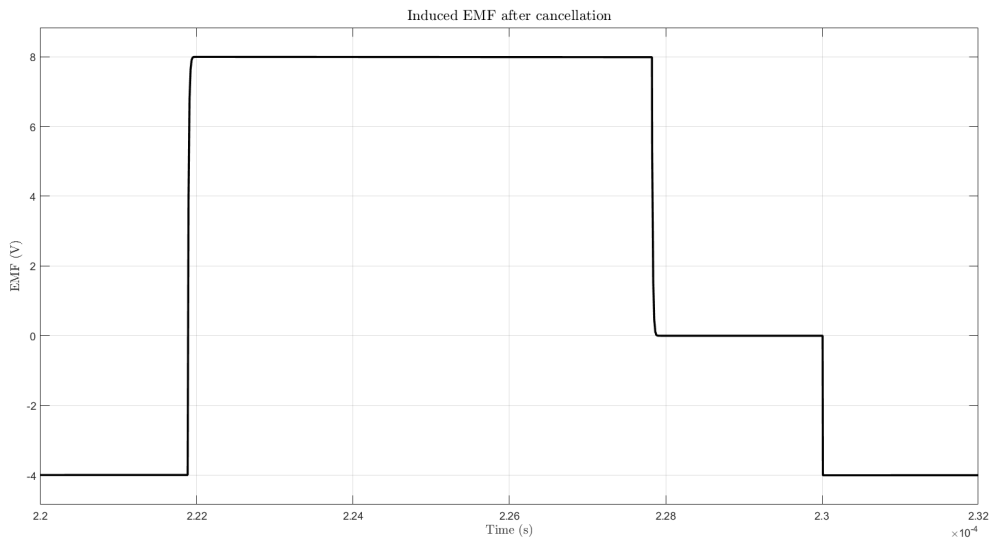


*Figure 3.24: Enhanced view of cancelled EMF waveform in open-loop topology.*

These results indicate a maximum voltage of  $V_{max} = 8 V$  and a minimum of  $V_{min} = -4 V$ . Since the polarity of the external magnetic field can be either positive or negative, the voltage supply rails of any selected amplifier should exceed  $\pm 10 V$  to avoid distortion due to clipping

### Chapter 3. Software Implementation

of the EMF signal. Furthermore, Figure 3.24 reveals that the minimum required slew rate of the amplifier in the two-core open-loop topology is:

$$\frac{\Delta V}{\Delta t} = \frac{7.97851 - (-3.99144)}{2.21947 \times 10^{-4} - 2.21883 \times 10^{-4}} \approx 200 \frac{V}{\mu s} \quad (3.24)$$

The induced EMF within the closed-loop topology differs significantly from that of its open-loop counterpart. In the closed-loop configuration, the EMF signal is continuously varying due to the presence of active feedback within the instrument. This behaviour reflects the system's ongoing effort to cancel the external magnetic field in real time. The corresponding waveform is shown in Figure 3.25, with a focused view provided in Figure 3.26.

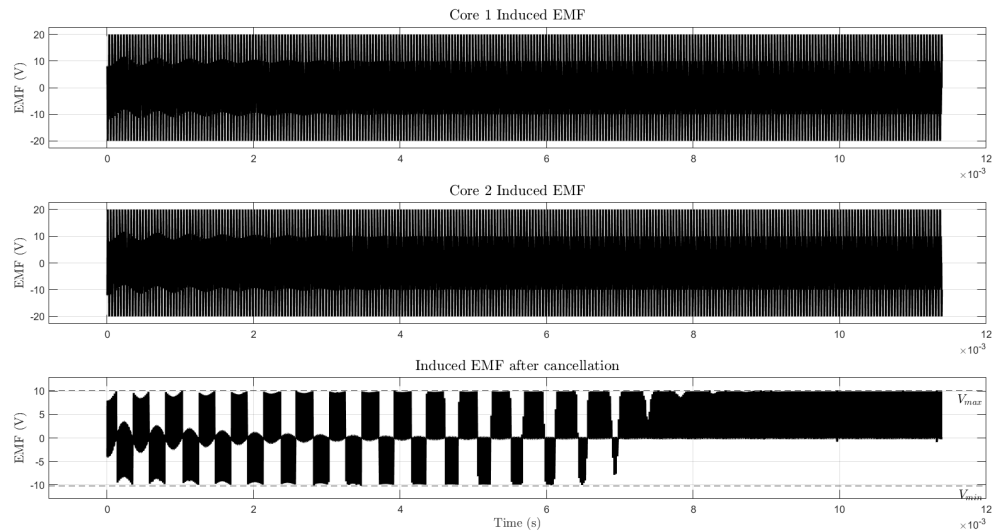


*Figure 3.25: Induced EMF waveforms of the two-core closed-loop topology given  $I_{ext} = 5 A$ .*

### Chapter 3. Software Implementation

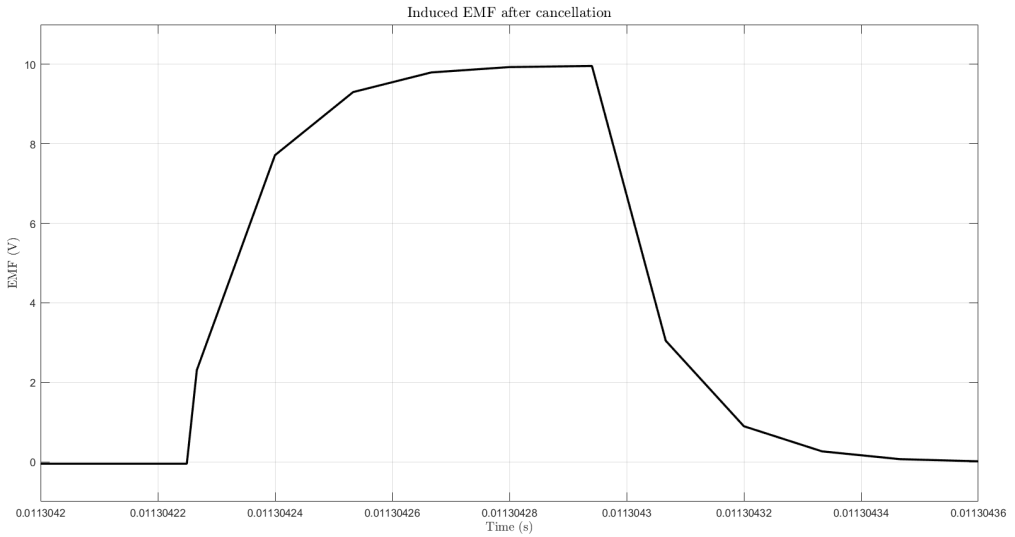


*Figure 3.26: Enhanced view of cancelled EMF waveform in closed-loop topology.*

The results show that the maximum and minimum voltage requirements remain the same as seen in the open-loop topology. As previously mentioned, the EMF waveform fluctuation is due to the feedback within the system due to the transient stage of the control attempting to match the external field. Once the control reaches steady state ( $V_{comp} = I_{ext}$ ) the EMF waveforms pattern becomes much more predictable and symbolises the required feedback to mitigate the external field. Investigating this signal further shows that for the steady state portion of the signal the slew rate requirements increase drastically. For no information loss, the closed-loop topology slew rate is:

$$\frac{\Delta V}{\Delta t} = \frac{2.30941 - (-0.0481083)}{1.1304227 \times 10^{-2} - 1.1304225 \times 10^{-2}} \approx 1.2 \frac{V}{ns} \quad (3.25)$$

This analysis implies that the components used within the peripheral circuitry require a dual supply voltage that exceeds  $\pm 10 V$  and an incredibly high slew rate for perfect signal processing.

### 3.5.3 Non-Ideal Testing

Given the constraints identified during the EMF waveform analysis, a parameter-based search was conducted to select a suitable amplifier for use within the peripheral circuitry. A decision matrix was developed to evaluate potential candidates based on key performance metrics such as slew rate, supply voltage range, and cost. This matrix is presented in Figure 3.27.

Description						
Component Name	Supply Voltage	Slew Rate	Availability	Price	Extra	
LM7171AIM/NOPB	+/- 18 V	4.1 kV/us	7187	3.54		
AD844JRZ-16-REEL7	+/- 18 V	2 kV/us	140	11.93		
LT1357CS8#TRPBF	+/- 18 V	600 V/us	9272	7.03	Unity-Gain Stable	
ADEL2020AR-20	+/- 18 V	500 V/us	10 week lead	10.07		
Ranking						
Component Name	Supply Voltage	Slew Rate	Availability	Price	Extra	Total
LM7171AIM/NOPB	5	5	4	5	0	19
AD844JRZ-16-REEL7	5	5	2	3	0	15
LT1357CS8#TRPBF	5	3	5	4	5	22
ADEL2020AR-20	5	3	0	3	0	11

Figure 3.27: Decision matrix for amplifier selection.

Based on this evaluation, the LT1357 high-speed operational amplifier [33] was selected as the most appropriate choice due to its ability to operate as a unity-gain buffer stage, allowing for greater flexibility and reduced variation in component selection. Using this amplifier along with the LTC1043 switching capacitor, a non-ideal simulation of the peripheral circuitry was created using LTspice, the circuit can be seen in Figure 3.28.

### Chapter 3. Software Implementation

**Open-Loop Two-Core Topology**

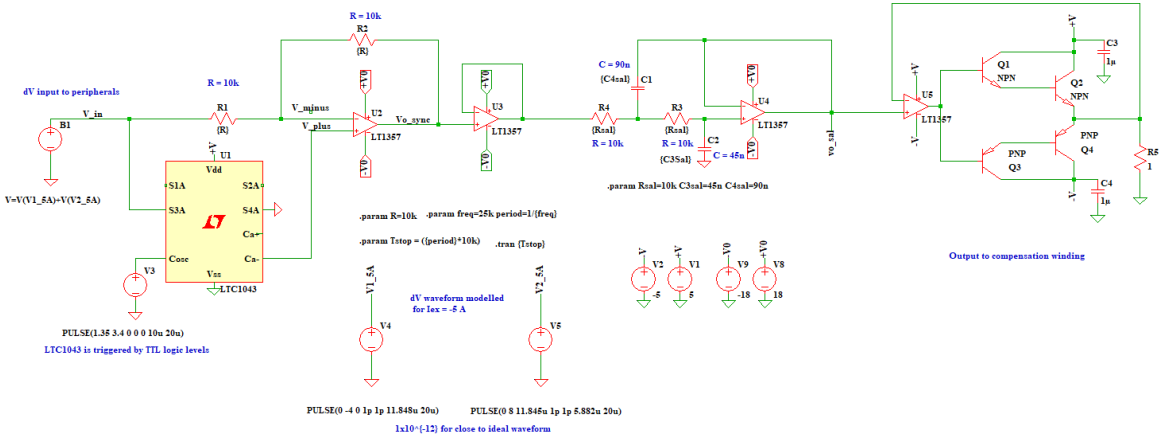


Figure 3.28: Peripheral circuitry LTspice implementation.

This circuit includes an input waveform designed to replicate the signal observed by the peripheral circuitry following induced EMF cancellation. The overall structure follows the same topology as the MATLAB implementation, however, the switch in the synchronous demodulator stage is replaced by the LTC1043 switched-capacitor block. This block is driven by an external clock using trip levels of  $V^+ = 3.4 V$  and  $V^- = 1.35 V$ .

In practical hardware, the LTC1043 also allows internal clock generation via an external capacitor connected between the  $C_{osc}$  and  $V_{ss}$  pins. The oscillator frequency based on this configuration is given in the datasheet as:

$$f_{osc} = 190 \times 10^3 \cdot \frac{24 \times 10^{-12}}{24 \times 10^{-12} + C_{ext}} \quad (3.26)$$

This feature provides an additional layer of configurability and safety in hardware implementation. When tested with an induced EMF waveform corresponding to  $I_{ext} = 5 A$ , the resulting output waveform is as shown in Figure 3.29.

### Chapter 3. Software Implementation

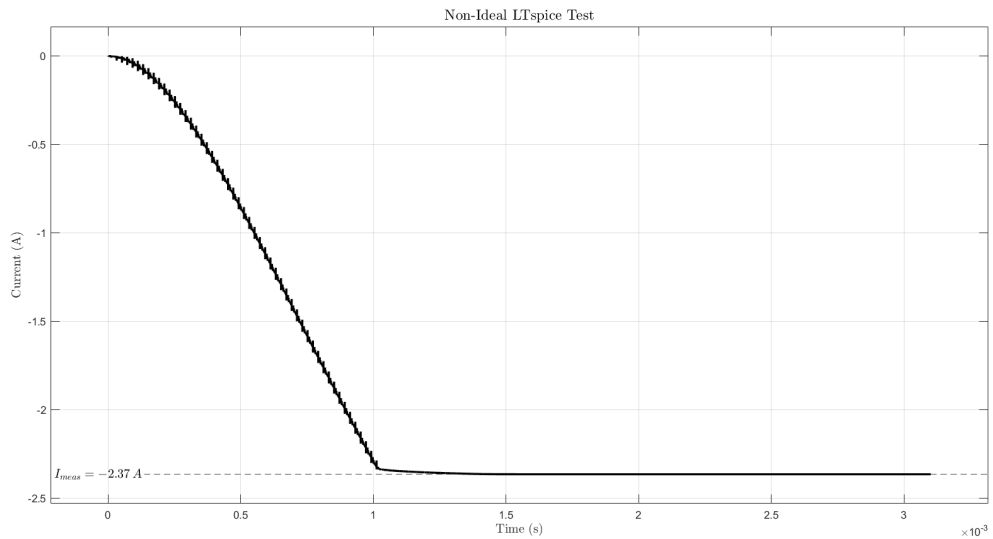


*Figure 3.29: Output of non-ideal LTspice test.*

As shown, the measured value is  $I_{meas} = -2.37 A$ , which is approximately half of the expected value of  $I_{meas} = -4 A$  obtained in the MATLAB implementation. To investigate the performance under this new condition, re-testing was conducted in MATLAB using compensation current values  $I_{comp} = -4 A$  and  $I_{comp} = -2 A$ . The resulting waveforms are presented in Figure 3.30.

### Chapter 3. Software Implementation

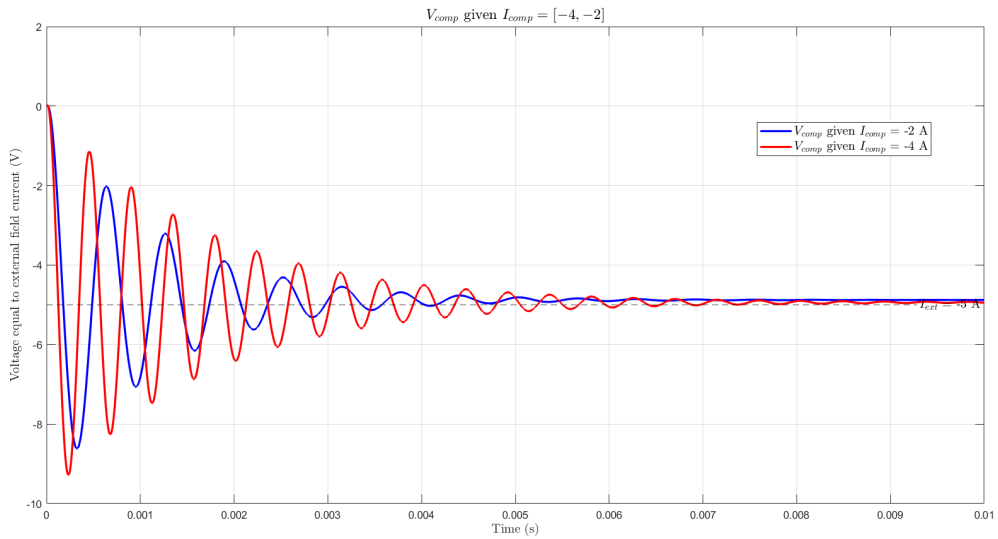


*Figure 3.30:  $I_{comp}$  test between ideal and non-ideal conditions.*

These results demonstrate that the non-ideal LTspice simulation actually achieves faster convergence to steady state compared to the ideal MATLAB model. Recalling that  $V_{comp}$  represents the directly measured current corresponding to the external magnetic field. The test results show that the steady-state value in the non-ideal case is  $V_{comp} = -4.88 \text{ V}$ , while the ideal case yields  $V_{comp} = -4.94 \text{ V}$ . This difference results in a reduced fluxgate accuracy of  $\eta = 97.6\%$  in the non-ideal simulation scenario. As the observed performance degradation was minimal in the fluxgate using non-ideal components, the transition to hardware implementation began.

## 4 Hardware Implementation

The hardware implementation of the fluxgate sensor documents the process of designing and assembling a printed circuit board (PCB) that integrates the peripheral circuitry. The layout of the PCB reflects the non-ideal conditions modelled in the LTspice simulation, as shown in Figure 3.28. This includes all components required for signal processing, closely following the topology validated in simulation.

### 4.1 Circuit Schematic

The PCB was designed using Fusion 360, which, compared to other industry-standard platforms such as Altium Designer offers a more limited component library. As a result, several key components used in the LTspice simulation were not available within the native library. To address this, a custom component library was developed, and each component was assigned a custom footprint based on mechanical specifications provided in the respective datasheets.

The components requiring custom footprints included: the LTC1043 (switched-capacitor block), the LT1357 (high-speed operational amplifier), the MJD127T4 [34] (selected PNP Darlington transistor), and the MJD6039T4G [35] (selected NPN Darlington transistor).

After the custom library was completed, the circuit schematic was created. Each integrated circuit powered by a voltage supply was paired with local decoupling capacitors to minimise voltage ripple and ensure a stable DC voltage at the supply pins. Additionally, five mounting pins were incorporated into the design to allow the PCB to be securely positioned as a free-standing unit. The circuit schematic blocks in Fusion 360 can be seen in Figures 4.1 - 4.6.

## Chapter 4. Hardware Implementation

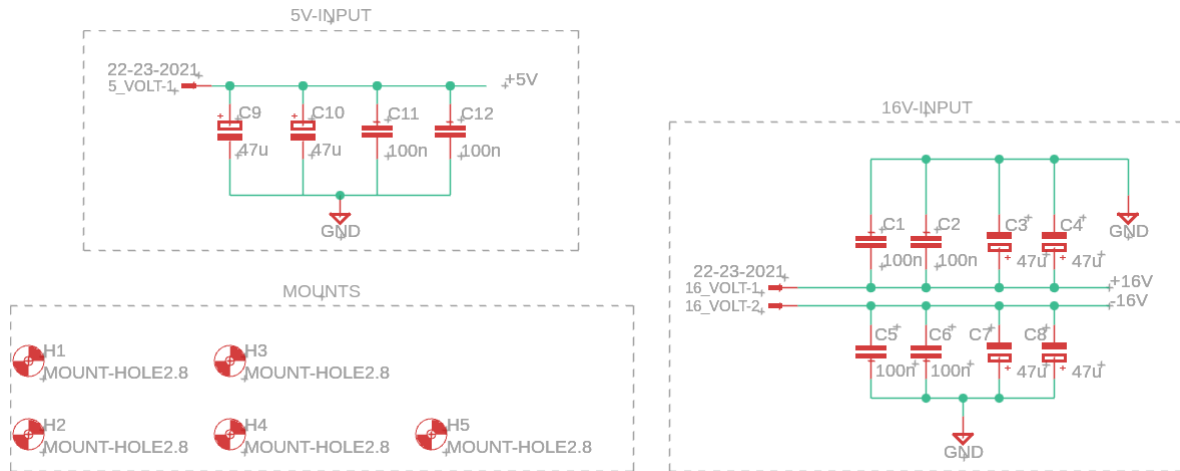


Figure 4.1: Input supply and mounting pins Fusion 360 implementation.

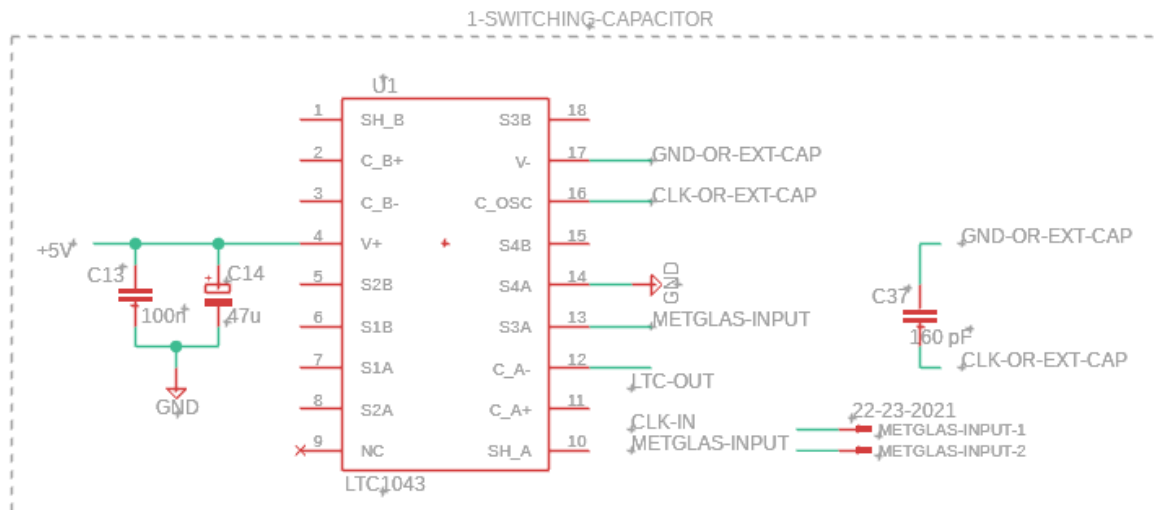


Figure 4.2: LTC1043 switched-capacitor Fusion 360 implementation.

## Chapter 4. Hardware Implementation

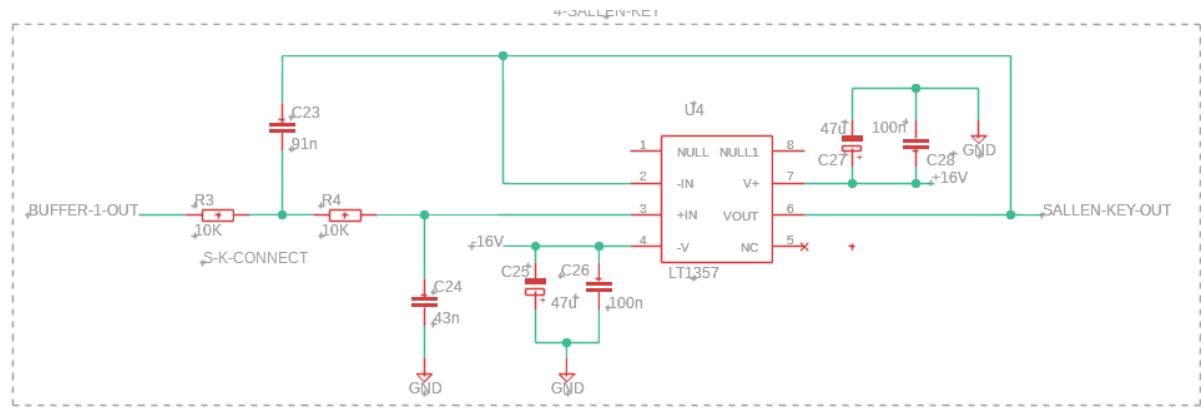


Figure 4.3: Synchronous demodulator Fusion 360 implementation.

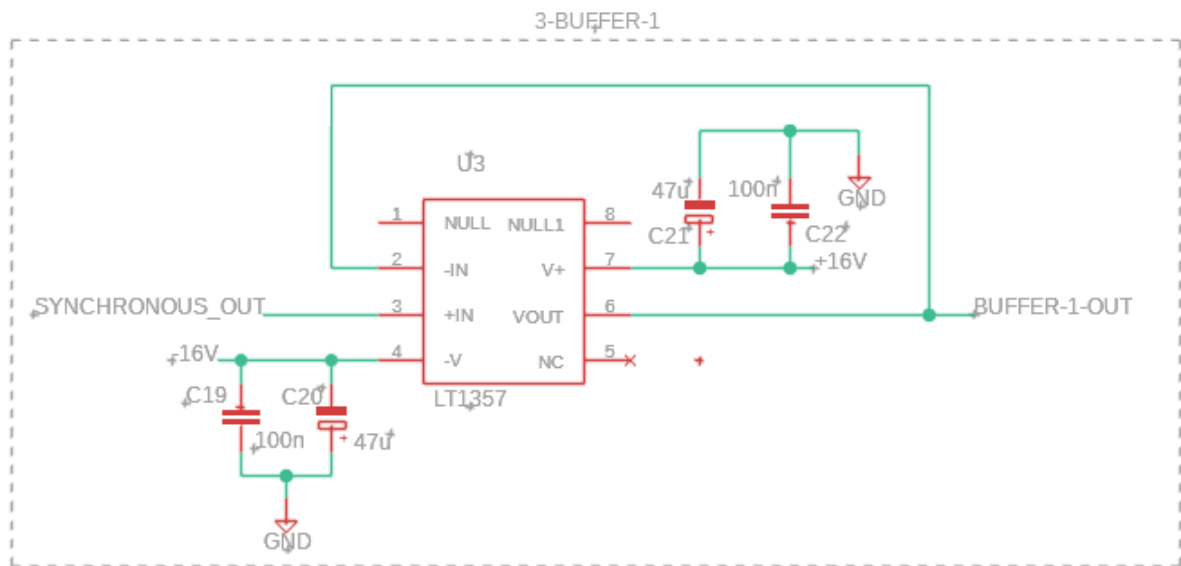


Figure 4.4: Buffer amplifier Fusion 360 implementation.

## Chapter 4. Hardware Implementation

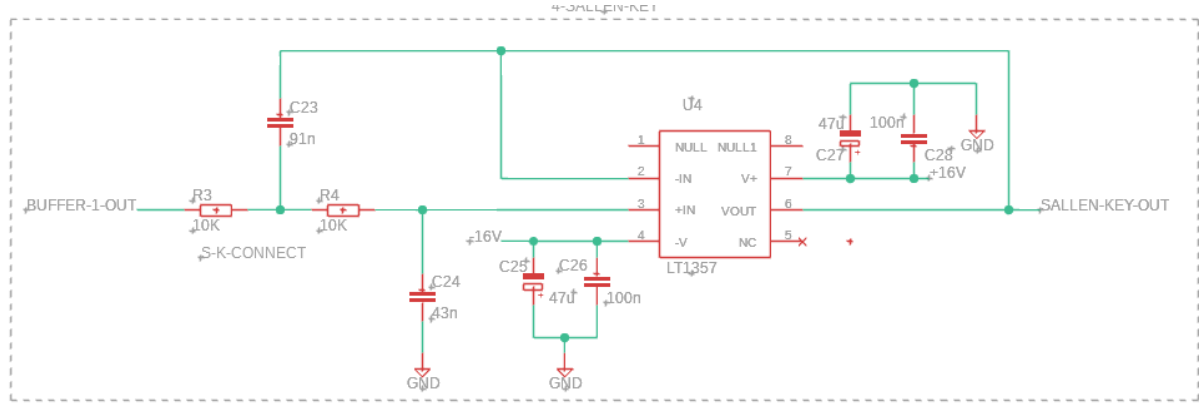


Figure 4.5: Sallen-key Fusion 360 implementation.

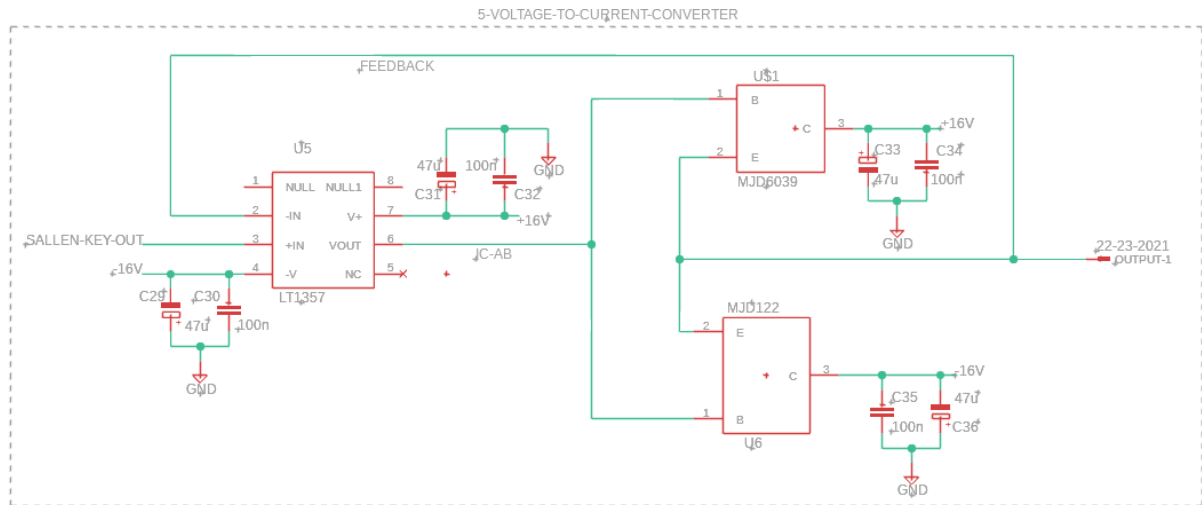


Figure 4.6: V-I amplifier Fusion 360 implementation.

## 4.2 PCB Schematic

Following the completion of the circuit schematic, the next step was to implement the design onto a PCB. During the layout process, several key resources were consulted [36] [37] [38] to ensure proper operation of the design. In addition to adhering to the core PCB layout guidelines and checklists outlined in these resources, test points were incorporated for each key component in the final PCB design (Orange - Signal, Black - Local Ground) to allow straightforward probe access during testing. Furthermore, several nearby ground test points were introduced to pro-

## Chapter 4. Hardware Implementation

vide local reference connections, improving measurement accuracy during hardware validation. An added precaution was implemented in the LTC1043 design, Figure 4.2. This precaution allows the LTC1043 to be driven by an external clock. However, to account for the possibility that external clocking may not function as intended during testing, the design also supports internal clock control via an external capacitor. The created PCB can be seen within Figure 4.7 and Figure 4.8.

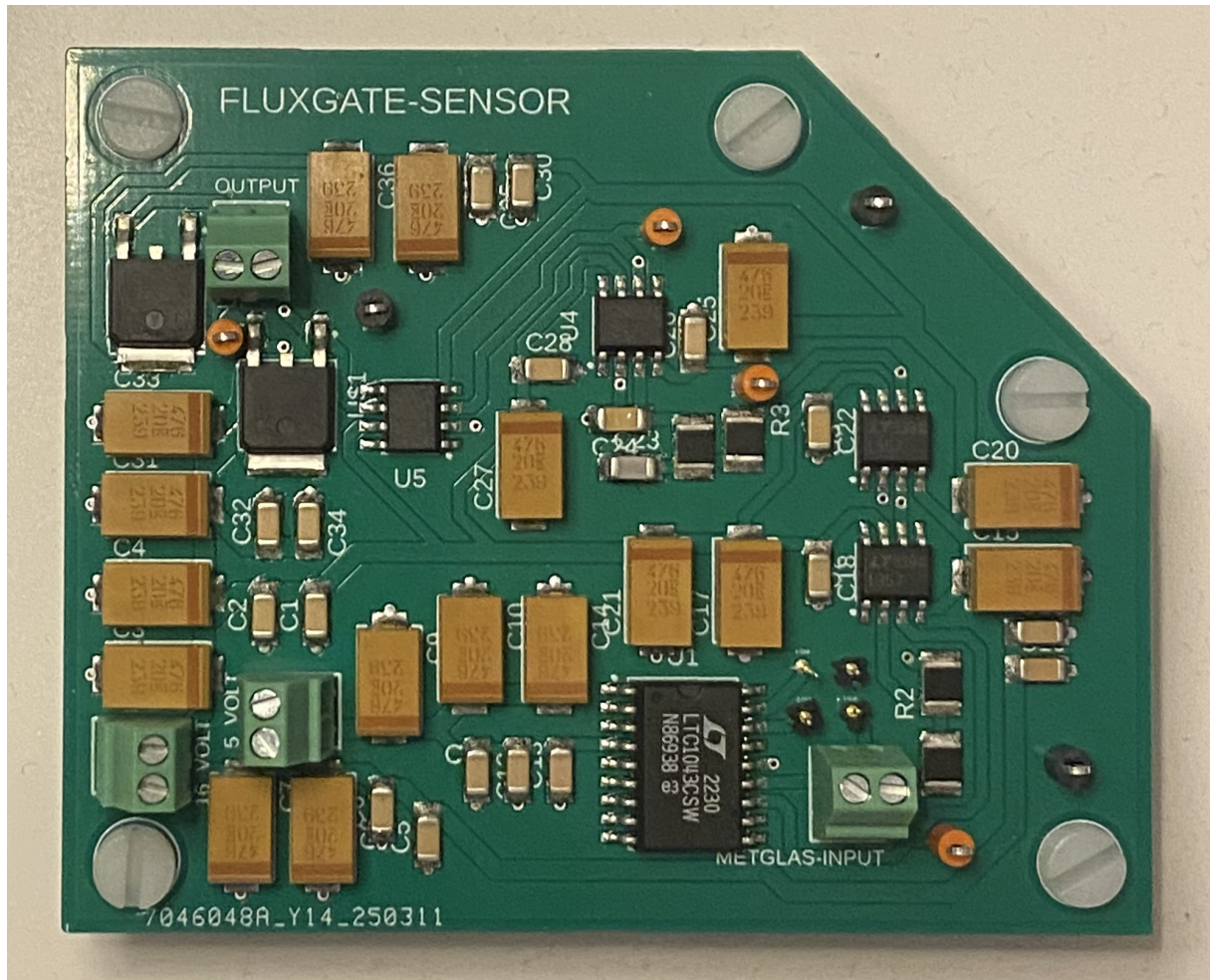


Figure 4.7: Designed PCB (top).

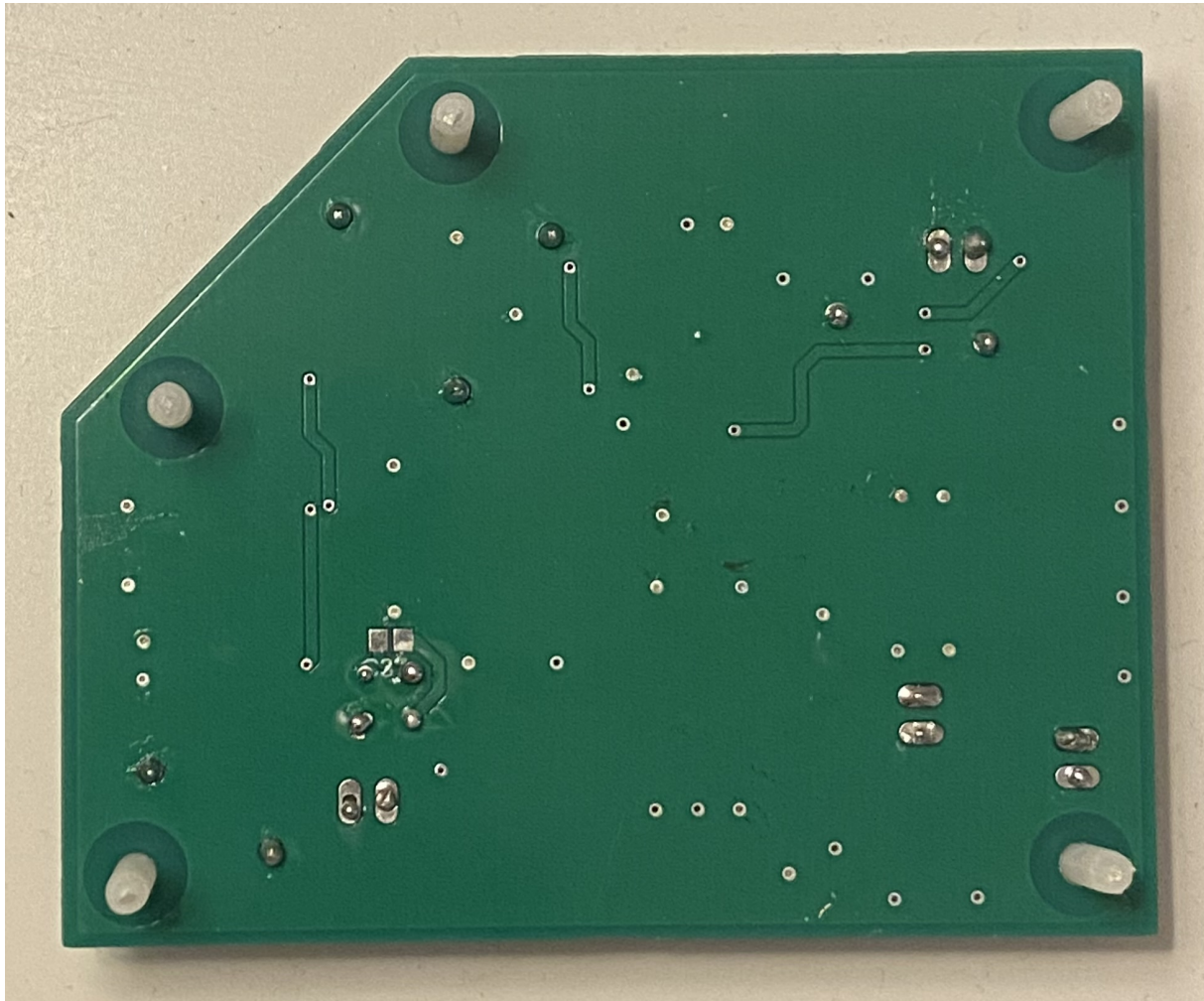


Figure 4.8: Designed PCB (bottom).

## 4.3 Hardware Testing

### 4.3.1 B-H Curve Test

The first experiment to evaluate the Metglas cores involved characterising their B-H curves. The setup for this test consisted of a function generator, a power amplifier (PA), a Metglas core, and a resistor. In this configuration, the input signal from the function generator was varied at a frequency of  $5\text{ kHz}$  and amplified by the PA with a gain of  $G = 2 \frac{A}{V}$ . The amplified signal was simultaneously connected to both Channel 1 of the oscilloscope and the Metglas core. Channel

## Chapter 4. Hardware Implementation

2 of the oscilloscope was used to measure the voltage drop across a  $15\Omega$  resistor placed in series with the core, enabling current monitoring through the core. Specifications for these modules are provided in Table 4.1. A schematic of the test configuration is shown in Figure 4.9, with the physical setup presented in Figure 4.10.

*Table 4.1: Summary of modules for B-H curve test.*

Module Name	Manufacturer Name	Manufacturer Part Number
Function Generator	Tektronix	AFG1022
Power Amplifier	Kepco and Kepco Power	BOP5-20DL
Oscilloscope	Teledyne Lecroy	WaveRunner 8058HD
$15\Omega$ Resistor	RS Pro	RS300 Mount Resistor

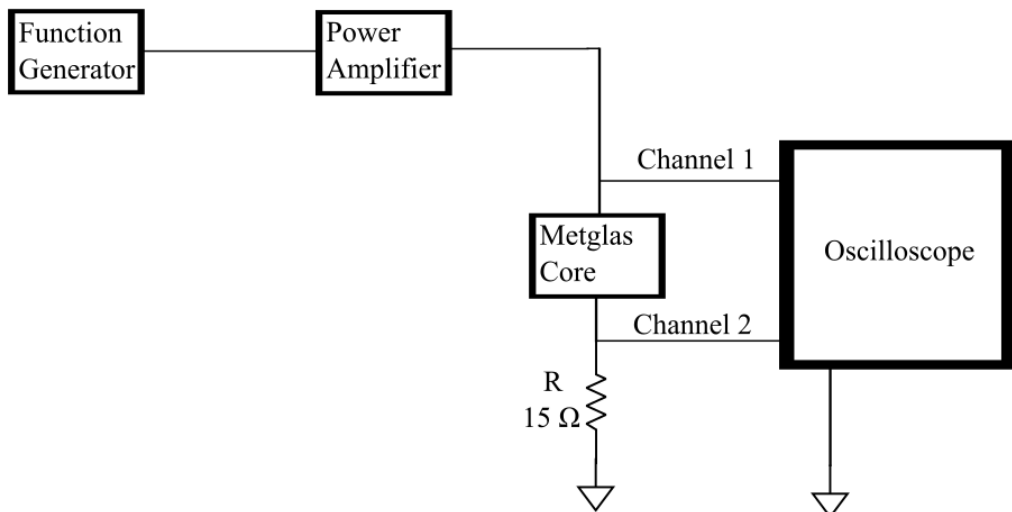


*Figure 4.9: B-H curve test setup schematic.*

## Chapter 4. Hardware Implementation

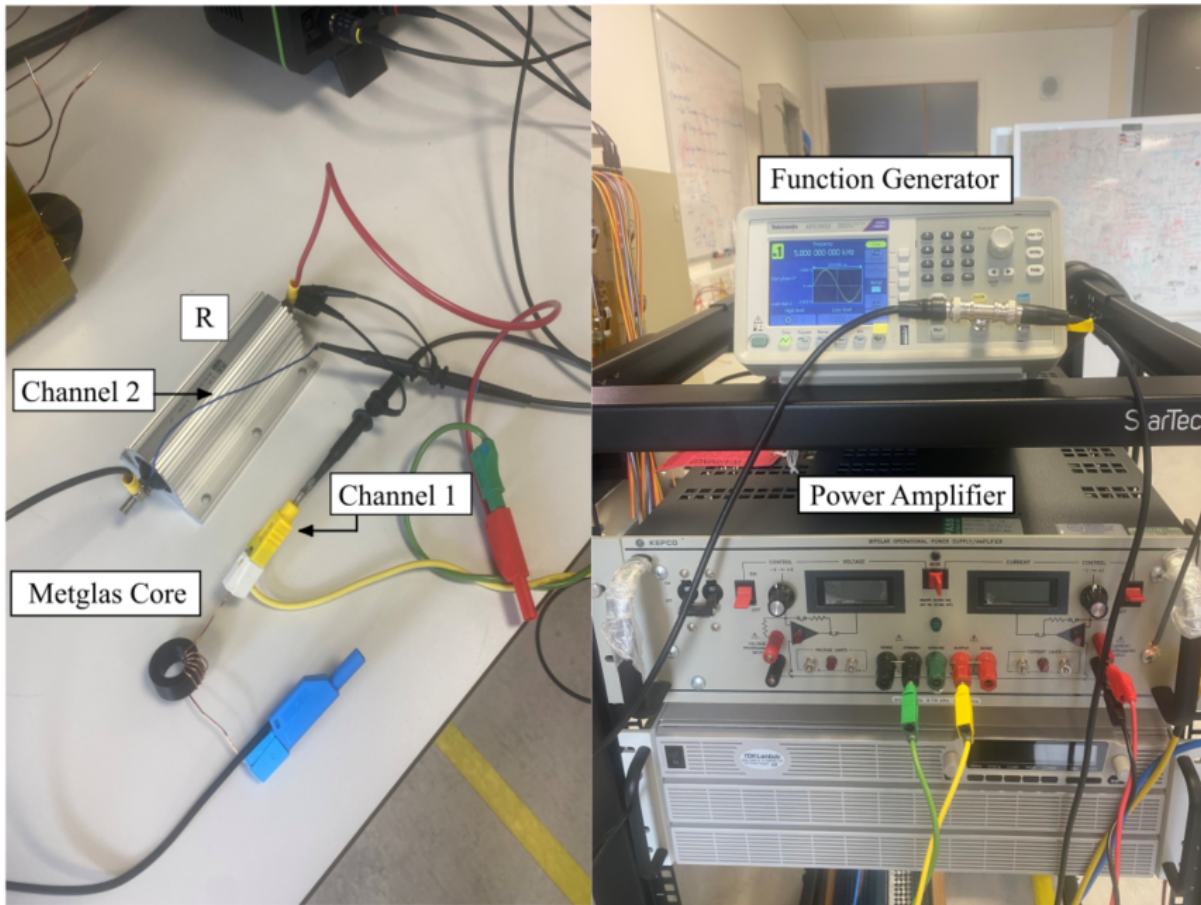


*Figure 4.10: B-H curve test practical setup.*

The extracted waveforms required further processing to reconstruct the core's B-H curve, the magnetic flux density  $B$  was obtained by:

$$B = \frac{1}{NA_e} \int V(Channel\ 1) - V(Channel\ 2) \quad (4.1)$$

While the magnetic field intensity  $H$  was calculated as:

$$H = \frac{NV(Channel\ 2)}{Rl_e} \quad (4.2)$$

This test was conducted using both sine and square waveforms as input excitation signals, for comparison across different voltage amplitudes: 10 mV, 50 mV, 100 mV, and 1 V. The

## Chapter 4. Hardware Implementation

resulting B-H curves for each case are shown in Figure 4.11 and Figure 4.12.

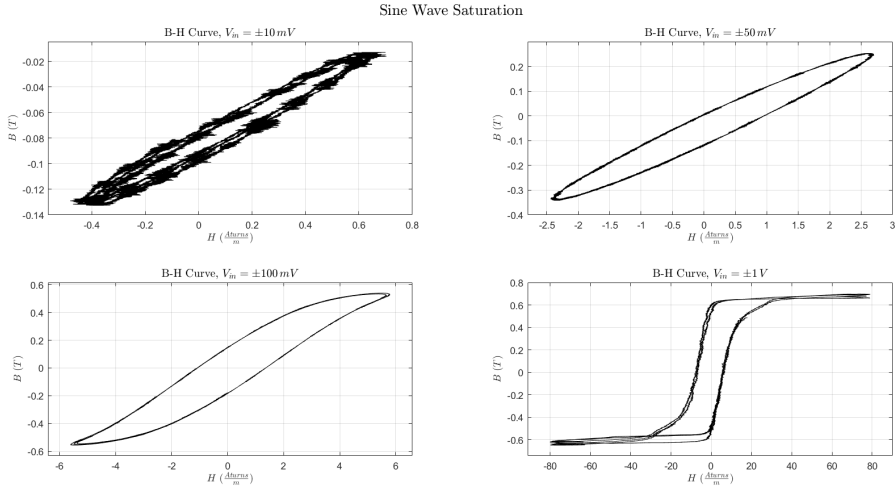


*Figure 4.11: B-H curve test with sine wave drive excitation.*

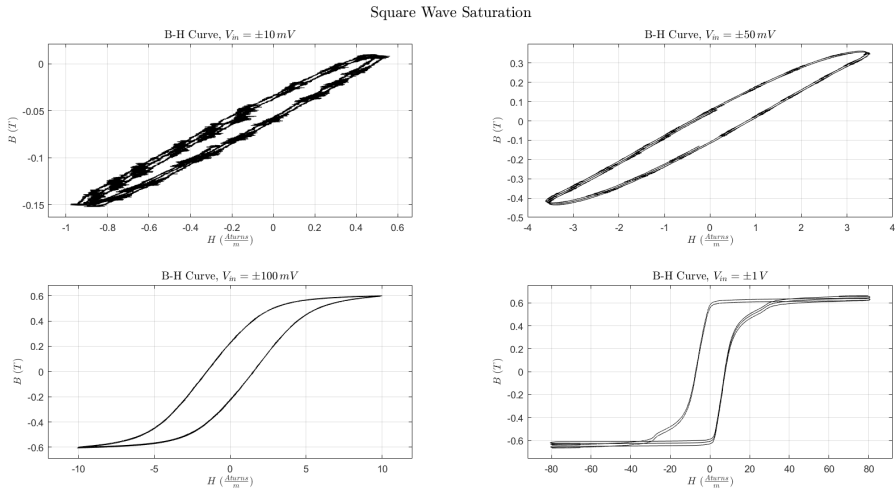


*Figure 4.12: B-H curve test with square wave drive excitation.*

The measured data clearly illustrates the characteristic B-H curve of the Metglas core. A slight offset is observed in some of the plots, which is most likely due to a DC bias introduced by the power amplifier during current control operation.

### 4.3.2 External Current Test

The second test of the Metglas cores serves the purpose of analysing the effect of an external current on the core. In this experiment the core was driven into saturation using a DSP C2000 microcontroller alongside a power amplifier to provide a square wave input with a duty cycle of 50% that follows the voltage of a DC power supply. To limit the current flowing through the core, a series resistor ( $15 \Omega$ ) was introduced, resulting in a maximum current defined by:

$$I_{limit} = \frac{V_{DC}}{15} A \quad (4.3)$$

An external magnetic field was applied by wiring a high-power DC current supply through the core. The effect of this external field was observed as a distortion in the symmetry of the core current waveform, which was visualized using an oscilloscope. The specifications of these modules are provided in Table 4.2. A schematic of the setup is shown in Figure 4.13, and the corresponding physical implementation is presented in Figure 4.14.

*Table 4.2: Summary of modules for external current test.*

Module Name	Manufacturer Name	Manufacturer Part Number
Microcontroller	Texas Instruments	DSP C2000
Power Amplifier	Texas Instruments	BOOSTXL-3PHGANINV
DC Supply	Tenma	72-2935
High-power Current Supply	EA Elektro-Automatik	EA-EL 9000 DT
Oscilloscope	Multicomp Pro	MP720105
Current Probe	AIM-TTI Instruments	IPROBER 520
$15 \Omega$ Resistor	RS Pro	RS300 Mount Resistor

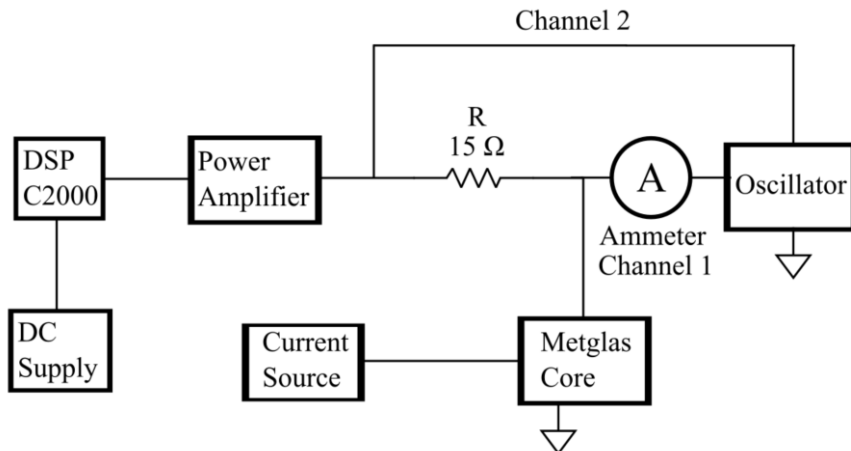


*Figure 4.13: External current test setup schematic.*

The results shown in Figure 4.15 demonstrate the fluxgate principle under a drive current of 4 A, highlighting how an external DC current influences the core's magnetic response. Specifically, the presence of an external current introduces a distortion in the core's saturation cycle, leading to a loss of symmetry in the waveform. This asymmetry gives rise to a second-harmonic component, which would be processed by the designed PCB to extract the magnitude of the external current.

In the oscilloscope capture, the input voltage waveform (blue) applied to the core appears as a periodic square wave, while the corresponding current waveform (yellow) exhibits the typical saturation behaviour of the core. As the external DC current increases, a clear shift in the symmetry of the current waveform is observed, consistent with the expected effect. This validates the operational principle of the fluxgate sensor and provides a visual representation of how an external magnetic field distorts the core's saturation cycle.

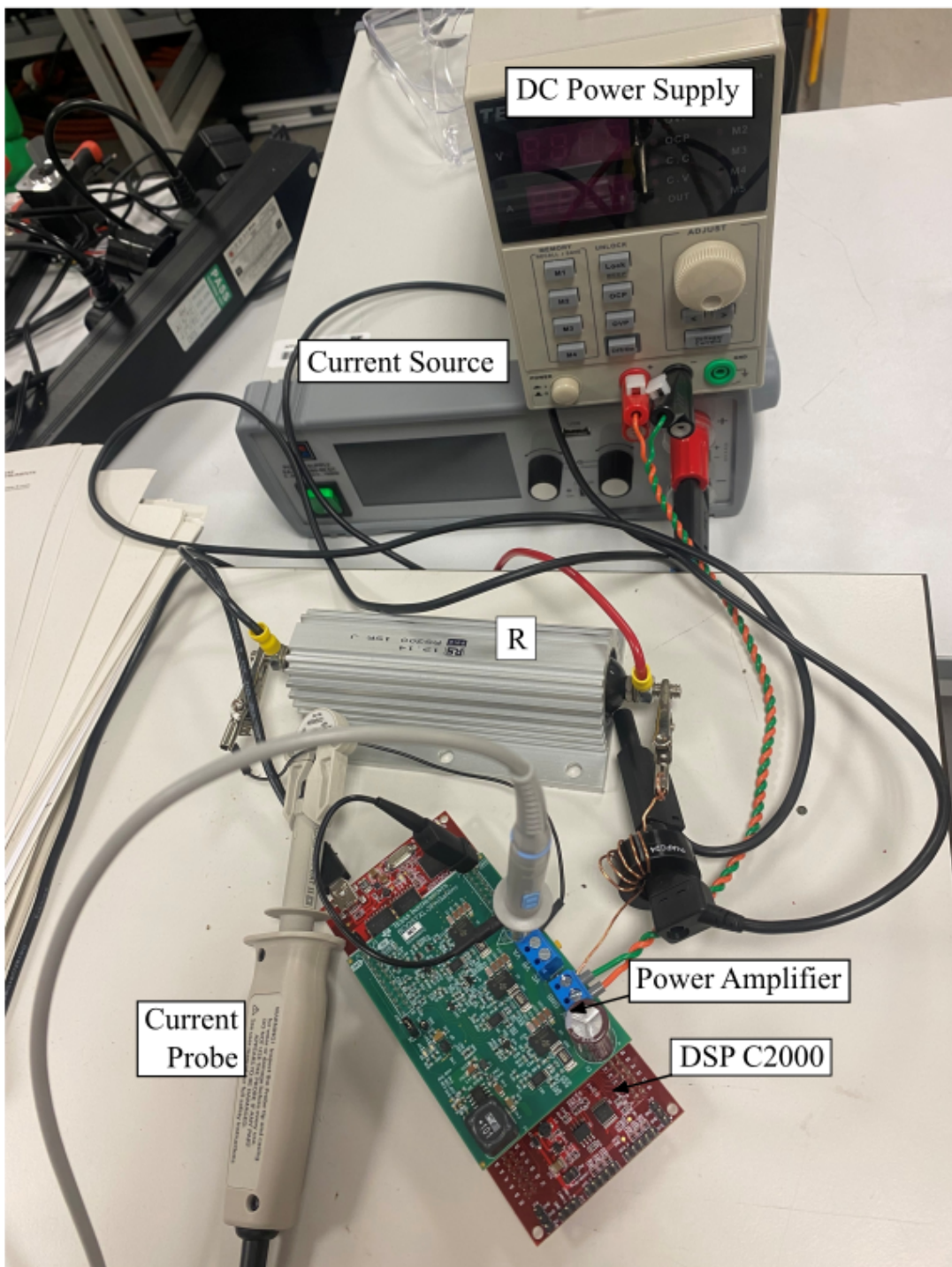


Figure 4.14: External current test practical setup.

## Chapter 4. Hardware Implementation

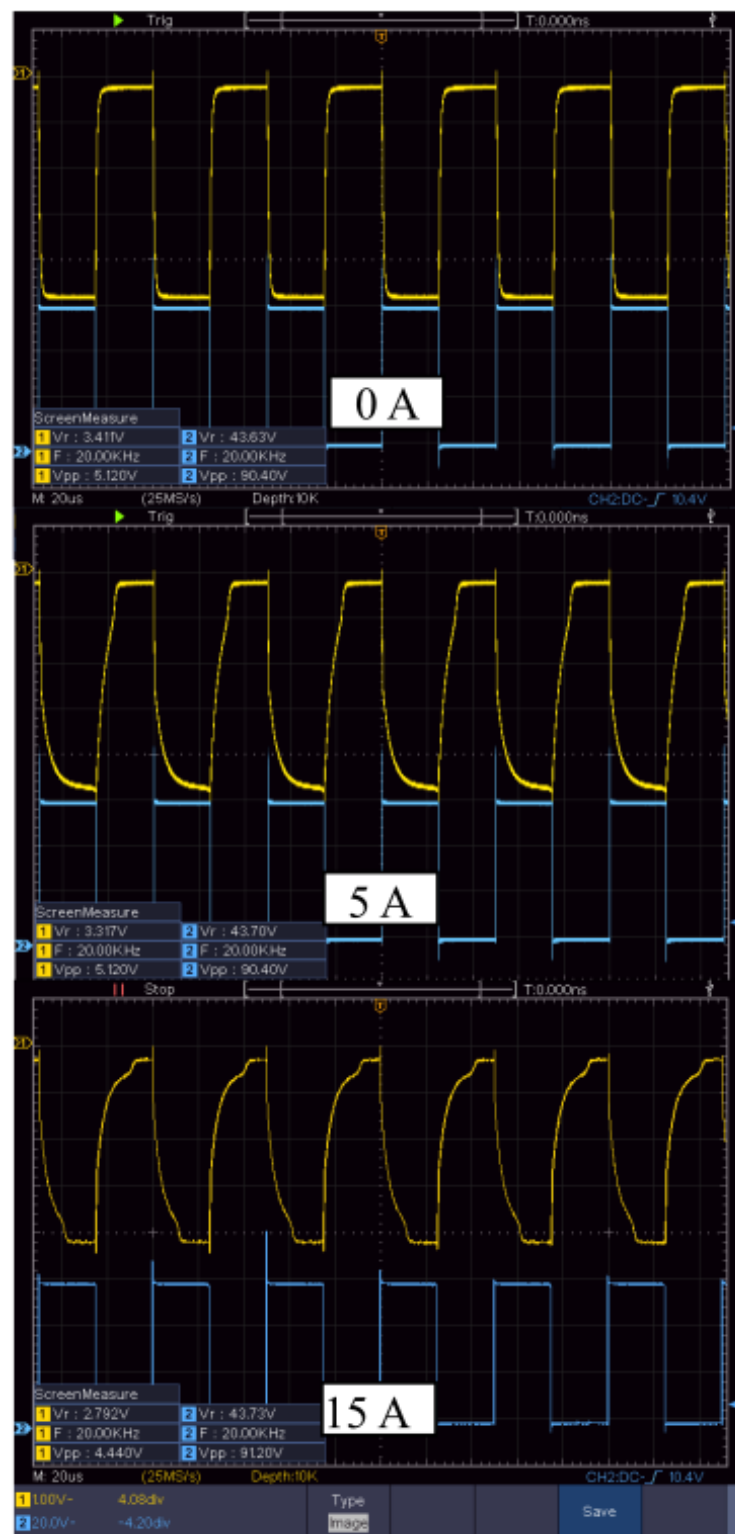


Figure 4.15: External current test results.

## 5 Discussion

This project provides a thorough understanding of the fluxgate operating principle, along with the successful design and simulation of various multi-core fluxgate topologies. Through iterative modelling and analysis, both open-loop and closed-loop configurations were explored, demonstrating the sensor's potential for accurate, non-contact current measurement in challenging environments.

The open-loop topologies of the fluxgate design demonstrate the intended functionality and maintain a linear response, confirming that the proportionality between the output signal and the external magnetic field remains intact. This validates the viability of open-loop configurations in software and suggests that they are practically applicable for measuring small external currents, provided that the sensor is tested with a known field to accurately determine the proportionality constant. However, a significant limitation of open-loop designs is the absence of feedback control within the circuit. As a result, these configurations lack the ability to actively cancel the external magnetic field, which significantly restricts their dynamic range. Experimental testing established the upper limit of the open-loop topology at an external current of  $I_{ext} = 8\text{ A}$ , beyond which the magnetic cores are no longer driven fully into saturation. This leads to a breakdown of the linear relationship between the fluxgate and the measured field, ultimately making the measurements taken in this region invalid.

In contrast, the closed-loop topology actively cancels magnetic interference by employing the feedback through a compensation winding that neutralizes the magnetic flux generated by external fields. This keeps the magnetic cores in a near-zero influence state, even when exposed to varying external magnetic influences. Because the core operates close to its zero-flux

## Chapter 5. Discussion

point, it becomes much more difficult to drive it into saturation. Significant changes in current magnitude or polarity are required to disturb this balanced state, which enhances the system's linearity and stability. It is also due to this closed-loop cancellation that slow moving AC fields can be measured with reduced accuracy. Figure 5.1 shows the closed-loop response to various AC external field inputs.

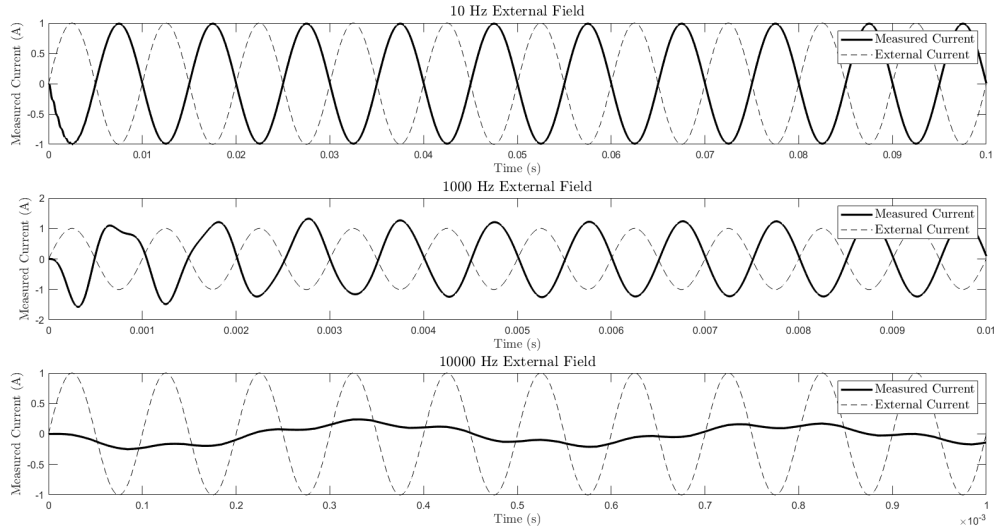


*Figure 5.1: Fluxgate AC field test.*

It can be observed that the performance of the fluxgate sensor degrades as the frequency of the external magnetic field increases. This degradation is primarily due to the fluxgate's limited bandwidth, which prevents it from accurately responding to rapid variations in the magnetic field.

At 10 Hz, the fluxgate performs optimally. The measured waveform closely matches the amplitude of the external field and maintains a consistent shape. This waveform is  $180^\circ$  out of phase with the original signal as it actively cancels the magnetic field by generating an opposing field in the Metglas cores through its feedback loop.

At 1000 Hz, the fluxgate can still track the waveform, but with a noticeable difference in amplitude. The sensor struggles to follow the external field waveform due to the increased rate of change in the external field signal. As a result, the compensation current causes overshoot,

## Chapter 5. Discussion

producing a measured signal with an elevated amplitude.

By 10 kHz, the external field frequency far exceeds the fluxgate's operational bandwidth. At this point, the sensor can no longer respond rapidly enough to track the field accurately. The result is a heavily damped output, where the measured current lags behind and under represents the actual field.

The closed-loop two-core topology exhibits important characteristics regarding the relationship between compensation winding accuracy and response time. A key observation is that increasing the number of turns in the compensation winding improves the accuracy of the instrument. This relationship can be described by the following expression:

$$I_{comp} = \frac{I_{ext}}{N_{comp}} \quad (5.1)$$

This equation demonstrates that as the number of compensation winding turns,  $N_{comp}$ , increases, the compensation current required to cancel the external current  $I_{ext}$  decreases proportionally. As a result, the sensor becomes capable of resolving finer increments of external current, thereby enhancing its sensitivity and measurement precision.

However, this increase in  $N_{comp}$  has a direct impact on the system's dynamic response, specifically the time required for the output signal to converge to steady state. This behaviour is maintained by the time constant of the magnetic core, defined as:

$$\tau = \frac{L}{R} \quad (5.2)$$

- L, Inductance of the compensation winding, H
- R, Series resistance of the winding, Ω

The inductance of a coil is defined as:

$$L = \frac{\mu N^2 A_e}{l_e} \quad (5.3)$$

## Chapter 5. Discussion

This equation shows that inductance increases with the square of the number of turns,  $N^2$ . Consequently, increasing  $N_{comp}$  enhances measurement accuracy but also increases the inductance and, in turn, the time constant  $\tau$ . This introduces a fundamental trade-off in fluxgate design between resolution and convergence speed, higher resolution via more turns results in slower system response. Figure 5.2 presents the results obtained for various values of compensation winding turns, illustrating the effect on both convergence time and measurement accuracy. It is important to note that for each test, the condition  $N_{comp} = R_{comp}$  was maintained to ensure proportional voltage scaling and preserve the direct relationship between the compensation voltage and external current.

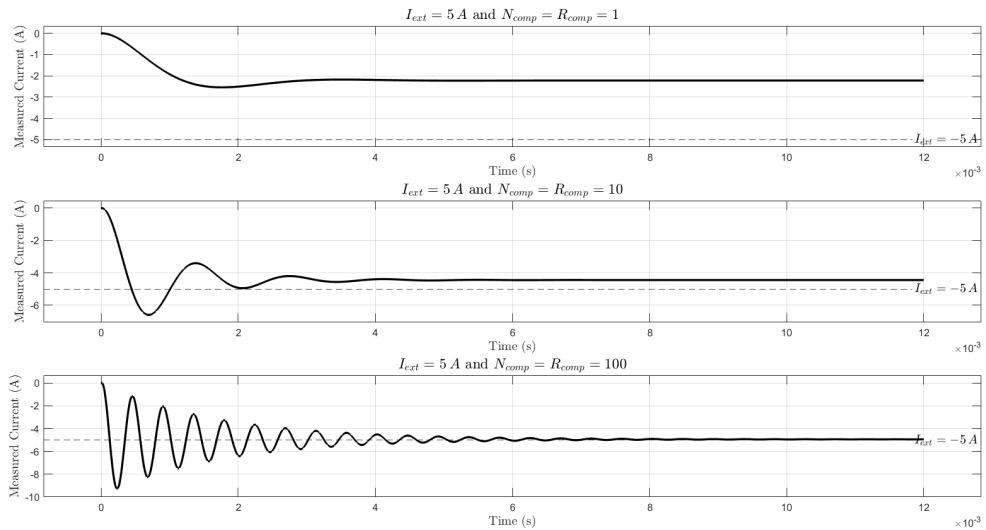


Figure 5.2: Compensation winding test.

These results help visualise the effect that the compensation winding turns has on accuracy and system response time.

Within the non-ideal simulations, the LT1357 operational amplifier which has a slew rate of  $600 \frac{V}{\mu s}$  was selected for implementation. As discussed in the non-ideal testing section, this choice introduces a limitation in the system's response, resulting in a slight reduction in overall accuracy. Despite this, the functionality of the fluxgate sensor remains unaffected. The implication of this constraint is that some information is temporarily lost due to the amplifier's inability

## Chapter 5. Discussion

to track rapid voltage changes at the speed required for perfect processing,  $1.2 \frac{V}{ns}$ . This loss acts as an accumulated error in the system, which continues to build until it reaches a threshold detectable by the sensor. At this point, the fluxgate is able to respond and apply corrective compensation. In short this effect explains the loss in accuracy observed within the non-ideal software implementation.

Also during non-ideal testing, the decision to utilise components from Analog Devices/Linear Technology significantly streamlined the simulation process. These manufacturers provide detailed LTspice models for many of their components, enabling immediate access to realistic behavioural characteristics without the need to manually construct custom models or extract parameters from datasheets. This greatly reduced development time and ensured a higher degree of simulation to hardware accuracy. As a whole, the results of the simulations portray an effective implementation of external current measurement of DC and slow varying fields.

In terms of the PCB design, the choice to include decoupling capacitors at each supply rail was made to ensure local voltage stability and suppress noise that may interfere with sensitive components. Decoupling capacitors provide instantaneous current to integrated circuits when there are transient loads, thus mitigating fluctuations within the main supply voltage. The effectiveness of a decoupling capacitor is not determined by its capacitance, but also by its equivalent series resistance (ESR) and its equivalent series inductance (ESL). These parasitic elements contribute to an increase in impedance at higher frequencies. In the absence of proper decoupling, high frequency noise may cause ripple and instability in the system. To address this, a parallel combination of tantalum and ceramic capacitors was employed, with the tantalum capacitor providing low-frequency bulk decoupling and the ceramic capacitor targeting high-frequency noise suppression [39] [40].

The B-H curve test of the Metglas cores was conducted using both a square wave and a sine wave to further evaluate the effect of the drive waveform choice on core saturation. Whilst both waveforms successfully drive the core into saturation, the square wave demonstrates a greater ability to push the core further into saturation at the same peak-to-peak voltage. This behaviour is illustrated in Figure 4.11 and Figure 4.12. An explanation of this difference is the effective

## Chapter 5. Discussion

power delivery of each waveform. Although both have the same peak-to-peak amplitude, the square wave maintains its maximum voltage for a longer portion of the cycle. As a result, it delivers a higher root-mean-square (RMS) voltage to the load in comparison to the sine wave. This leads to a greater average current through the core and a stronger resulting magnetic field intensity. This explains the difference in field intensity within the waveforms. Furthermore the graph shows that the core enters saturation around the suspected saturation flux density ( $B_{sat} = 0.57 T$ ).

The external current test further demonstrates the characteristic waveform distortion observed in fluxgate operation under the influence of an external magnetic field, further validating the viability of the Metglas core within hardware implementation.

## 6 Conclusion

This project set out to design and implement a fluxgate current sensor capable of reliable operation in cryogenic environments, such as those encountered in superconducting systems and aerospace applications. The outcomes contribute meaningfully to the development of non-contact current sensing technologies suited to extreme thermal conditions. In addition to its technical contribution, the project aligns with the UN SDGs, supporting advancements in the electrification of aircraft and space-based technologies to promote sustainability within the aerospace sector.

The design of the fluxgate current sensor began with a detailed understanding of the complex principles of fluxgate operation, established through an extensive literature review. This led to the evaluation of various core topologies and drive methods, ultimately resulting in the choice of using Metglas toroidal cores driven by a square wave input. Analysis of fluxgate behaviour was explored through the utilisation of LTspice and MATLAB/Simulink, enabling the development of high-level circuit models that accurately reflected the physical operation of a fluxgate.

Simulink was further utilised to implement expanded topologies, including multi-core designs and open-loop configurations, incorporating realistic peripheral circuitry. These simulations revealed a clear proportional relationship between the sensor output and applied external magnetic fields, further consolidating the understanding of fluxgate operation. Continued development of these models resulted in a two-core closed-loop topology, which achieved high accuracy through the introduction of a feedback loop via a compensation winding.

LTspice was employed to evaluate real-world performance by simulating non-ideal conditions using component models provided by Analog Devices/Linear Technology. This process

## Chapter 6. Conclusion

streamlined practical component selection and enabled the evaluation of realised circuit behaviour. The simulations revealed a slight reduction in measurement accuracy compared to ideal conditions, decreasing from 98.8% → 97.6%, while maintaining full functionality.

A detailed review of PCB design was conducted, resulting in the development of a custom design containing the necessary electrical circuitry to perform signal processing for the Metglas cores. Experimental testing was conducted to evaluate the magnetic characteristics and performance of the cores, successfully validating the principles of fluxgate operation. However, due to time constraints, full integration and testing of the complete fluxgate system was not feasible within the project time frame.

Due to the complexity of the project, several reductions in the original project scope were necessary. These included the development of a two-core topology in place of the three-core configuration, as well as the adoption of CMOS-based integrated circuits instead of discrete components to improve compatibility with cryogenic temperatures (less than  $-150^{\circ}\text{C}$ ).

### 6.1 Further Work

Further work for this project includes the integration of additional peripheral circuits to reduce setup complexity. For example, incorporating a frequency halver or doubler would eliminate the need for an external clock or signal generator to produce the required second-harmonic reference. Building on this, the implementation of phase detection and signal matching would enable accurate measurement of moderate to high-frequency AC magnetic fields. This enhancement would require peripherals such as a lock-in amplifier to operate in place of the synchronous demodulator, facilitating the extraction of both amplitude and phase information from the induced signal. In parallel, a third-core topology could be introduced to expand the control bandwidth of the sensor.

The inclusion of a third core serves as a high-frequency feedback element [25]. Unlike the first two cores, which are driven into magnetic saturation to enable second-harmonic detection, the third core is not actively driven. Instead, it passively detects and responds to high-frequency

## Chapter 6. Conclusion

components of the external magnetic field. A schematic representation of this three-core topology is shown in Figure 6.1.

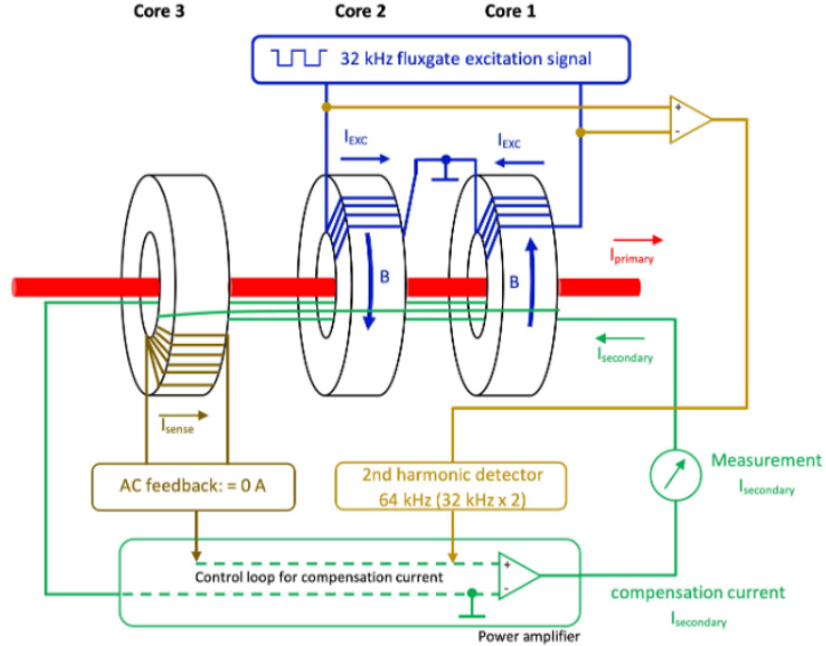


Figure 6.1: Three core fluxgate by Roland Bürger [25]

Recalling the expression for the induced electromotive force in a magnetic core:

$$\varepsilon = N A_e \frac{dB}{dt} \quad (6.1)$$

This highlights the third core's sensitivity to the rate of change of magnetic flux density. Under DC or low-frequency conditions,  $\frac{dB}{dt} \approx 0$ , and thus the induced EMF in the third core is negligible. However, as the frequency of the external field increases, the term  $\frac{dB}{dt}$  becomes significant, resulting in a non-zero EMF that directly reflects the external signal. During this moderate to high-frequency range, the third core has the ability to drive the feedback with its induced waveform, effectively enhancing the sensor's dynamic response.

At extremely high frequencies, the response time and bandwidth of the existing peripheral circuitry are exceeded. In this regime, the interaction between the third core and the compensa-

## Chapter 6. Conclusion

tion winding approximates transformer-like behaviour, where the external current is expressed in terms of turns-ratio compensation:

$$I_{comp}N_{comp} = I_{ext}N_{ext} \quad (6.2)$$

Assuming  $N_{ext} = 1$ , this simplifies to:

$$I_{comp} = \frac{I_{ext}}{N_{comp}} \quad (6.3)$$

This demonstrates that, even in high-frequency domains, the fluxgate sensor delivers a consistent result, comparable to that observed under DC or slowly varying field conditions. Thus, the integration of a third core provides an optimal solution for mitigating bandwidth limitations and ensures the sensor remains effective across a broad range of frequencies.

Another critical point for future development is the full validation of the hardware through experimental testing. As the sensor could only be partially evaluated in a laboratory setting, its real-world functionality has yet to be confirmed. This testing phase is critical for verifying complete operational reliability, assessing performance, and identifying any discrepancies between simulation and physical behaviour. The remaining tests involve integrating the two-core configuration with both drive and sense windings, followed by signal analysis using the custom-designed PCB. Initial tests should be conducted under open-loop conditions to evaluate signal integrity and core behaviour. Once validated, a compensation winding can be introduced to transition the system into closed-loop operation, enabling analysis of stability, accuracy, and real-time field cancellation. These steps are vital for confirming the sensor's complete functionality and ensuring alignment between theoretical models and practical implementation.

The final key priority for future development is adapting the sensor for full compatibility with cryogenic environments. This involves replacing all CMOS based integrated circuits with discrete component equivalents and conducting testing in a simulated cryogenic environment through the use of liquid nitrogen (-196 °C) to evaluate critical changes in performance and functionality due to temperature change.

## References

- [1] P. Ripka, *Magnetic Sensors and Magnetometers, Second Edition*, 2021.
- [2] N. Ness, “Magnetometers for space research,” *Space Science Reviews*, vol. 11, pp. 459–554, 10 1970.
- [3] J. S. Bennett *et al.*, “Precision magnetometers for aerospace applications: A review,” *Sensors*, vol. 21, no. 16, 2021. [Online]. Available: <https://www.mdpi.com/1424-8220/21/16/5568>
- [4] C. T. Russell *et al.*, “The Magnetospheric Multiscale Magnetometers,” *Space Science Reviews*, vol. 199, no. 1-4, pp. 189–256, March 2016. [Online]. Available: <https://ui.adsabs.harvard.edu/abs/2016SSRv..199..189R>
- [5] Supply design limited ltd. Accessed: [12/12/2024]. [Online]. Available: <https://www.supplydesign.com/>
- [6] Airbus. (2021) Cryogenics and superconductivity for aircraft explained. Airbus. Accessed: [24-03-2025]. [Online]. Available: <https://www.airbus.com/en/newsroom/stories/2021-03-cryogenics-and-superconductivity-for-aircraft-explained>
- [7] H. Gui, R. Chen, J. Jiahao, Z. Zhang, L. Tolbert, B. Blalock, D. Costinett, and B. Choi, “Review of power electronics components at cryogenic temperatures,” *IEEE Transactions on Power Electronics*, vol. PP, pp. 1–1, 10 2019.
- [8] A. Hammoud, R. Patterson, S. Gerber, and M. Elbuluk, “Electronic components and circuits for extreme temperature environments,” 01 2004, pp. 44 – 47 Vol.1.

## References

- [9] United Nations. Sustainable development goals. Accessed: [12/12/2024]. [Online]. Available: <https://sdgs.un.org/goals>
- [10] European Commission. 2050 long-term strategy. Accessed: [12/12/2024]. [Online]. Available: [https://climate.ec.europa.eu/eu-action/climate-strategies-targets/2050-long-term-strategy\\_en](https://climate.ec.europa.eu/eu-action/climate-strategies-targets/2050-long-term-strategy_en)
- [11] F. Primdahl, “The fluxgate magnetometer,” *J. Phys. E: Sci. Instrum.*, vol. 12, no. 4, pp. 241–253, 1979.
- [12] J. Lenz and S. Edelstein, “Magnetic sensors and their applications,” *IEEE Sensors Journal*, vol. 6, no. 3, pp. 631–649, 2006.
- [13] Y. Sheiretov, “Deep penetration magnetoquasistatic sensors,” 05 2005.
- [14] J. Vcelak, P. Ripka, and A. Zikmund, “Precise magnetic sensors for navigation and prospection,” *Journal of Superconductivity and Novel Magnetism*, vol. 28, 03 2014.
- [15] A. Balogh, “Planetary magnetic field measurements: Missions and instrumentation,” *Space Science Reviews*, vol. 152, pp. 23–97, 05 2010.
- [16] M. H. Acuña, “Space-based magnetometers,” *Review of Scientific Instruments*, vol. 73, no. 11, pp. 3717–3736, 11 2002. [Online]. Available: <https://doi.org/10.1063/1.1510570>
- [17] C. Zhang, Y. Zhang, and X. Wang, “Study of nonlinear excitation circuits for fluxgate magnetometer,” 02 2023.
- [18] P. Baranov, V. Baranova, A. Kolomeytsev, and I. Zatonov, “Drive signal waveform for a fluxgate,” *Journal of Physics: Conference Series*, vol. 1065, p. 052020, 08 2018.
- [19] S. V. Marshall, “An analytic model for the fluxgate magnetometer,” *IEEE Transactions on Magnetics*, vol. MAG-3, pp. 459–463, September 1967.

## References

- [20] A. Ostaszewska-Liżewska and R. Szewczyk, “Method of moments based modelling of race-track fluxgate sensitivity dependence on track and core width,” *Acta Physica Polonica A*, vol. 137, pp. 697–699, 05 2020.
- [21] G. Musmann and Y. Afanassiev, *Fluxgate Magnetometers for Space Research*, 2010.
- [22] E. Billingsley and S. Billingsley, “Fluxgate magnetometers,” *Proceedings of SPIE - The International Society for Optical Engineering*, vol. 5090, 09 2003.
- [23] (n.d.) Fluxgate current sensors. Accessed: [28/11/2024]. Published by LEM. [Online]. Available: <https://www.lem.com/en/fluxgate-current-sensors>
- [24] U. Platise, M. Achim, and E. Kalšek, “Integrated power measurement solution with patented high-performance ac/dc current transducer,” *IRT3000 News*, March 2021, accessed: [11/12/2024]. [Online]. Available: [https://www.irt3000.si/en/news/2021032913272746/integrated\\_power\\_measurement\\_solution\\_with\\_patented\\_highperformance\\_acdc\\_current\\_transducer/](https://www.irt3000.si/en/news/2021032913272746/integrated_power_measurement_solution_with_patented_highperformance_acdc_current_transducer/)
- [25] R. Bürger. (2022, sep) Ct's - fluxgate vs. inductive. Published by SENSELEQ on Electrical Engineering Academy. Accessed: [28/11/2024]. [Online]. Available: <https://electrical-engineering.academy/posts/cts-fluxgate-vs-inductive>
- [26] TDK Electronics AG, “SIFERRIT material T38,” 2013, accessed: [14-03-2025]. [Online]. Available: <https://www.tdk-electronics.tdk.com/download/528868/c2cb0f1f5413cd8e83b8ecf7e85152f9/pdf-t38.pdf>
- [27] Metglas, Inc., “Magnetic alloy 2714a (cobalt-based),” 2011, accessed: [14-03-2025]. [Online]. Available: [https://www.mouser.co.uk/datasheet/2/957/magamp\\_opt-1509990.pdf](https://www.mouser.co.uk/datasheet/2/957/magamp_opt-1509990.pdf)
- [28] S. Oliveira da Silva and R. Modesto, “A comparative analysis of srf-based controllers applied to active power line conditioners,” 12 2008, pp. 405 – 410.

## References

- [29] Linear Technology, *LTC1043: Dual Precision Instrumentation Switched-Capacitor Building Block*, 2007, accessed: [18-03-2025]. [Online]. Available: <https://www.analog.com/media/en/technical-documentation/data-sheets/1043fa.pdf>
- [30] I. Thlama Balami, E. Anene, A. Muhammad, M. Ahmed, and S. Kumo, “Identified optimal infinite impulse response filters for eight band audio equalizer using bacterial foraging algorithm (bfa),” vol. 5, pp. 1–7, 08 2021.
- [31] Texas Instruments, “Opa860 wide bandwidth operational transconductance amplifier (ota) and buffer,” August 2008, sBOS331C. [Online]. Available: <https://www.ti.com/lit/ds/symlink/opa860.pdf>
- [32] ——, “Voltage-to-current (v-i) converter circuit with a darlington transistor,” May 2021, application Report SBOA326. [Online]. Available: <https://www.ti.com/lit/an/sboa326/sboa326.pdf>
- [33] Linear Technology Corporation, *LT1357 - 25MHz, 600V/ $\mu$ s Op Amp*, 1994, datasheet. [Online]. Available: <https://www.analog.com/media/en/technical-documentation/data-sheets/1357fa.pdf>
- [34] STMicroelectronics, *MJD122, MJD127 - Complementary Power Darlington Transistors*, April 2009, document ID 3541, Rev. 11. [Online]. Available: <https://www.st.com/resource/en/datasheet/mjd127.pdf>
- [35] onsemi, *MJD6039 - Darlington Power Transistors*, December 2024, data Sheet, Rev. 10, Publication Order Number: MJD6039/D. [Online]. Available: <https://www.onsemi.com/pdf/datasheet/mjd6039-d.pdf>
- [36] Sierra Circuits, *High-Speed PCB Design Guide*, 2020, design publication on high-speed PCB layout and signal integrity considerations. [Online]. Available: <https://s3vi.ndc.nasa.gov/ssri-kb/static/resources/High-Speed%20PCB%20Design%20Guide.pdf>

## References

- [37] D. L. Jones, *PCB Design Tutorial*, June 2004, revision A. [Online]. Available: [https://www.scs.stanford.edu/~zyedidia/docs/pcb/pcb\\_tutorial.pdf](https://www.scs.stanford.edu/~zyedidia/docs/pcb/pcb_tutorial.pdf)
- [38] L. W. Ritchey and J. Zasio, *Right the First Time: A Practical Handbook on High Speed PCB and System Design*, revised 9/15/08 ed. Santa Clara, CA: Speeding Edge, 2003, edited by Kella J. Knack.
- [39] Sierra Circuits. (2021, March) What is the use of a decoupling capacitor? Accessed: [26-03-2025]. [Online]. Available: <https://www.protoexpress.com/blog/decoupling-capacitor-use/>
- [40] Texas Instruments, “Notes on decoupling capacitors,” [https://www.ti.com/content/dam/videos/external-videos/en-us/9/3816841626001/6313253251112.mp4/subassets/notes-decoupling\\_capacitors.pdf](https://www.ti.com/content/dam/videos/external-videos/en-us/9/3816841626001/6313253251112.mp4/subassets/notes-decoupling_capacitors.pdf), n.d., accessed: [26-03-2025].